


System analysis based on the cancer–immunity cycle identifies ZNF207 as a novel immunotherapy target for hepatocellular carcinoma

Xu Wang,^{1,2} Tao Zhou,¹ Xingyi Chen,¹ Yu Wang,¹ Yushi Ding,¹ Haoyang Tu,¹ Shengyang Gao,¹ Haoyu Wang,¹ Xinying Tang,^{1,3} Yong Yang ^{1,3}

To cite: Wang X, Zhou T, Chen X, *et al.* System analysis based on the cancer–immunity cycle identifies ZNF207 as a novel immunotherapy target for hepatocellular carcinoma. *Journal for ImmunoTherapy of Cancer* 2022;**10**:e004414. doi:10.1136/jitc-2021-004414

► Additional supplemental material is published online only. To view, please visit the journal online (<http://dx.doi.org/10.1136/jitc-2021-004414>).

XW, TZ and XC contributed equally.

Accepted 07 February 2022



© Author(s) (or their employer(s)) 2022. Re-use permitted under CC BY-NC. No commercial re-use. See rights and permissions. Published by BMJ.

¹State Key Laboratory of Natural Medicines, China Pharmaceutical University, Nanjing, Jiangsu, China

²Jiangsu Center for the Collaboration and Innovation of Cancer Biotherapy, Cancer Institute, Xuzhou Medical University, Xuzhou, Jiangsu, China

³Department of Basic Medicine and Clinical Pharmacy, China Pharmaceutical University, Nanjing, Jiangsu, China

Correspondence to

Professor Yong Yang;
yy@cqu.edu.cn

Dr Xinying Tang;
1620174466@cqu.edu.cn

ABSTRACT

Background Immune checkpoint inhibitors as monotherapies for advanced hepatocellular carcinoma (HCC) fail to achieve satisfying results, while combination therapies show greater efficacy. Therefore, identifying new combined targets for immune checkpoint inhibitors could be promising.

Methods We combined the cancer–immunity cycle score with weighted gene coexpression network and system analyses to screen immunosuppressive targets in HCC. In vitro and in vivo experiments were used to assess the effect of zinc finger protein 207 (ZNF207) on HCC immunity. RNA sequencing, metabolomic, cytokine array analysis, dual-luciferase reporter gene assay, and ChIP quantitative PCR assay were used to investigate the role of ZNF207 in tumor immunity regulation.

Results The system analysis and experimental verification revealed ZNF207 as an immunosuppressive target in HCC. Hypoxia-induced upregulation of ZNF207 promoted HCC progression in immunocompetent mice while being associated with decreased CD8⁺ T-cell infiltration and increased exhaustion. Mechanistically, the mitogen-activated protein kinase (MAPK)–chemokine C-X3-C-motif ligand axis was involved in ZNF207-mediated CD8⁺ T-cell chemotaxis. Furthermore, ZNF207 transcriptionally regulated indoleamine 2,3-dioxygenase 1 and elevated kynurenine levels, leading to the exhaustion of CD8⁺ T cells. Patients with lower *ZNF207* expression were more sensitive to anti-programmed cell death protein 1 (PD1) therapy, and silencing *ZNF207* could be beneficial to anti-PD1 combination therapy.

Conclusion Our study implicates ZNF207 in suppressing the HCC microenvironment and showed the feasibility of targeting ZNF207 during anti-PD1 therapy in HCC.

INTRODUCTION

Hepatocellular carcinoma (HCC) is the third leading cause of cancer-related mortalities globally and a major threat to public health.¹ In first-line and second-line clinical settings, phase III clinical trials failed to show the survival benefits of immune checkpoint blockade agents for the treatment of unresectable HCC.^{2,3} The objective response rates

range between 15% and 20% when using these agents as monotherapies for HCC.⁴ The main limitations of existing immune checkpoint blockade therapies stem from multiple immune checkpoint pathways, as well as the lack of tumor infiltration by immune cells, and excessive exhaustion of immune cells.^{5–8} Several preliminary large phase III trials (eg, ORIENT-32, COSMIC-312, and HIMALAYA) used anti-PD1 or anti-programmed death-ligand 1 (PD-L1) agents combined with anti-CTLA4 or antiangiogenic agents (ie, combination therapies) and reported better survival compared with sorafenib monotherapy for unresectable HCC.^{9–11} Thus, the identification of new immune checkpoints and developing new combination treatments have become the major focus of HCC immunotherapy studies.

A comprehensive understanding of cancer–immunity interactions is essential for screening new targets for combination therapy. The cancer–immunity cycle elucidates on antitumor immune responses and offers an opportunity to understand the interactions between cancer and its immune system.¹² It can be used to visualize personalized antitumor immune responses in patients with HCC, which is correlated with their clinical outcomes.¹³ Based on the current findings, we tried to combine the cancer–immunity cycle score with bioinformatics to systematically explore immunosuppressive targets in HCC. The gle2-binding-sequence (GLEBS) motif-containing zinc finger protein 207 (ZNF207) obtained in our systematic analysis is a member of the ZNF protein family, which plays an essential role in self-renewal, pluripotency, and differentiation of human embryonic stem cells.^{14–16} HCC cells have elevated expression of *ZNF207*, which is associated with poor prognosis.¹⁷ However,

the mechanisms by which ZNF207 accelerates HCC progression are unknown, and its role in tumor immunity has not been established.

In this study, we systematically combined bioinformatic methods with experimental techniques to evaluate the immunosuppressive target ZNF207 in HCC in vitro and in vivo. Furthermore, we verified its potential as a biomarker and combination target for antiprogrammed cell death protein 1 (PD1) therapy. Lastly, we investigated the role of abnormal ZNF207 expression in HCC and its mechanism in accelerating HCC progression in terms of CD8⁺ T-cell regulation. This study will elaborate our understanding of the mechanisms activating HCC progression, as well as provide potential therapeutic targets for treatment and prognosis of HCC.

METHODS

Data and resources

The GDC download tool (<https://portal.gdc.cancer.gov>) from the Cancer Genome Atlas (TCGA) database was used to download the transcriptome data and clinical data for liver cancer (TCGA-liver hepatocellular carcinoma, LIHC). The fragments per kilobase million format expression data was used for subsequent expression-related analysis; the eight liver cancer microarray datasets (GSE14520, GSE17856, GSE25097, GSE36376, GSE45114, GSE54236, GSE64041, and GSE76427) can be downloaded from the GEO database (<https://www.ncbi.nlm.nih.gov/geo/>). When multiple probes correspond to the same gene symbol, the mean value was considered the final value, and all data were normalized by log₂.

WGCNA and hub gene screening

The R software 'WGCNA' package was used to construct a weight coexpression network. Normalized LIHC transcriptome expression data was used as a data matrix for WGCNA. The cancer-immunity cycle scores of HCC samples were obtained from the TIP database (<http://biocc.hrbmu.edu.cn/TIP/>) as clinical phenotypes for subsequent WGCNA. A fit β value=10 was selected to ensure the coexpression network is a scale-free network. The expression matrix was converted into an adjacency matrix and then converted into a topological matrix. Based on the topological overlap, the average-linkage hierarchical clustering method was used to cluster genes. According to the standard of the hybrid dynamic shearing tree, the minimum number of genes in each gene network module was set to 30. The eigengenes of each module were calculated, the modules clustered, and height set to 0.25; the gray module comprises genes that cannot be clustered into other modules. According to the eigengenes of each module, the correlation between these modules and each phenotype was calculated; the module phenotype correlation heat map was pictured; and modules with higher correlation were selected for subsequent analysis.

The protein-protein interaction (PPI) network of the interesting modules was constructed using Cytoscape v3.2.1, and then the topology heterogeneity of each node in the PPI network was analyzed. The degree value of each node was used to evaluate its importance. Finally, 10 nodes with the largest degree value in the network were selected. Simultaneously, analyzing the correlation between the genes and modules of interest, genes with a correlation >0.9 were selected. Genes meeting both the above two criteria were defined as hub genes.

Antibodies and reagents

Anti-ZNF207 (PA5-53535, PA5-30641, #703747) and anti-CD3z (4B10) (MA5-15608) antibodies were purchased from Invitrogen (Waltham, Massachusetts, USA). Anti-beta actin (ab8226) antibody was purchased from Abcam (Cambridge, UK). Anti-HIF-1 α (D1S7W; #36169), anti-HIF-2 α (D6T8V; #59973), anti-CD8 α (D4W2Z; #98941), and anti-PCNA (PC10; 2586) antibodies were purchased from Cell Signaling Technology (Danvers, Massachusetts, USA). Mouse C-X3-C-motif ligand (CX3CL1)/fractalkine chemokine domain antibody (MAB571) was purchased from R&D Systems (Minneapolis, Minnesota, USA). Anti-glyceraldehyde 3-phosphatedehydrogenase (GAPDH) (UPS002) was purchased from Upsbiotech. Mouse anti-PD1 (BE0146) and rat IgG2a isotype control antibody (BE0089) were purchased from Bio X Cell (Lebanon, New Hampshire, USA). Bay 87-2243 (S7309), PT2385 (S8352), PF-06840003 (S8657), and SB203580 (S1076) were purchased from Selleck (Houston, Texas, USA).

Animals and tumor implantation

C57BL/6N, BABL/c, and BABL/c-nude male mice (6 weeks old, 18–20 g) were purchased from Beijing Vital River Laboratory Animal Technology and housed in a specific pathogen-free environment with a 12/12 hour day/night cycle.

To establish the subcutaneous xenograft tumor model, HCCLM3 was subcutaneously inoculated with 2×10^6 cells/mouse on the right flank of BABL/c-nude mice. PLC/PRF/5 was subcutaneously inoculated with 5×10^6 cells/mouse, and Hepa1-6 was subcutaneously inoculated with 2×10^6 cells/mouse on the right flank of C57BL/6 mice. The tumor size was measured every 3 days using a digital caliper (Guanglu, Taizhou City, China). Tumor volume was calculated using the formula $(\text{length} \times \text{width}^2) / 2$.

For adeno-associated virus intervention, male BABL/c mice (6 weeks old, 18–20 g) were used. The mouse ascites tumor cells H22 with luciferase fluorescence were inoculated into the liver envelope of BABL/c mice at a concentration of 1×10^5 cells/mouse to construct a mouse liver orthotopic tumor model. After 3 days of inoculation, animal chemiluminescence imaging was performed, and the mice were grouped according to the fluorescence value. In vivo imaging observation was performed 3 weeks after the intervention, before the mice were sacrificed, and liver tumors were photographed.

Proteome profiler assay (cytokine array)

Hepa1-6-shNC and Hepa1-6-shZNF207 (5×10^6) were cultured in 10 cm dishes for 48 hours and the cell supernatant was harvested. The cells were then washed with phosphate buffered saline (PBS), lysed with IP lysate, and centrifuged at $12000g$ for 10 min. However, conditioned media and the supernatant of cell lysates were assayed using the R&D Systems Proteome Profiler Mouse XL Cytokine Array kit (ARY028) according to the manufacturer's instructions.^{18,19} Protein concentration was normalized before starting the assay. Chemiluminescence was detected by a charge-coupled device (CCD) camera (ChemiDoc MP; Bio-Rad, Hercules, California, USA). The pixel density of each spot was measured using ImageJ. The spots were averaged; the background was subtracted; and the average values were reported for each cytokine.

ChIP quantitative PCR assay (ChIP-qPCR)

To measure the binding activity of ZNF207 or indoleamine 2,3-dioxygenase 1 (IDO1) in vivo, a ChIP assay was conducted with the SimpleChIP Plus Enzymatic Chromatin IP Kit (#9005, CST) according to the manufacturer's protocol of 8024 cells. Briefly, 1×10^7 cells were cultured in hypoxia condition (1% O_2) for 24 hours or transfected with ZNF207-OE plasmid for 48 hours, then washed twice in PBS, crosslinked with formaldehyde, lysed with sodium dodecyl sulfate buffer, and sonicated. After sonication, the fragmented chromatin was added into ChIP dilution buffer and incubated overnight with anti-HIF1 α (CST, 36169, USA) and anti-HIF2 α monoclonal antibody (#59973, CST) or anti-ZNF207 (#703747, Invitrogen). A normal rabbit IgG (#2729, CST) was added as a negative control antibody, and the histone H3 rabbit monoclonal antibody was used as a positive control. Immunoprecipitated products were collected after incubation with protein A+G-coated magnetic beads. The bound chromatin was eluted and digested with proteinase K, then the DNA was purified for RT-qPCR analysis (the primers are listed in online supplemental materials and methods).

Statistical analysis

All data analyses were done using GraphPad Prism V.8 or SPSS V.19. Two-tailed Student's t-tests were performed when only two groups were compared. The paired t-test was used to analyze the difference in ZNF207 expression between 50 paired HCC samples. One-way analysis of variance followed by Dunnett's post-tests was used to compare differences between multiple groups unless otherwise stated. The χ^2 test was used to analyze the relationship between ZNF207 and clinical indices. Pearson's analysis was used for correlation analysis. Kaplan-Meier analysis was used for the survival analysis.

Additional experimental procedures are described in the online supplemental materials and methods.

RESULTS

ZNF207 is a potential immunosuppressive target in HCC

To find potential immunosuppressive targets in HCC, we used the cancer-immunity cycle scores and HCC transcriptome data for WGCNA network analysis. Cluster analysis divided all genes into 20 modules. Then, we conducted correlation analysis on all modules which revealed two clusters with similar internal expression patterns (figure 1A). Further analysis found modules in cluster 1 were positively correlated with steps 1-4 of the cancer-immunity cycle, while modules in cluster 2 were negatively correlated with steps 5-7 (figure 1B). Consistently, higher cancer-immunity cycle scores can be observed from steps 5 to 7 of the cycle in the ZNF207^{low} expression group (online supplemental figure S1A). Respectively, brown and turquoise were the modules with the most significant differences in clusters 1 and 2. To figure out the functions of these two modules, we performed Gene Ontology annotation analysis. Unsurprisingly, genes in the brown module were enriched in immune-related signaling pathways which show a positive correlation with steps 1-4 of the cancer-immunity cycle (figure 1C), while genes in the turquoise module were mainly enriched in RNA transport, RNA splicing, and spindle assembly processes which show negative correlation with steps 5-7 of the cancer-immunity cycle (figure 1D). Although it has been reported that the RNA splicing process is related to immunity,²⁰ its involvement in the immune process is still unclear. To identify immunosuppressive targets in HCC, we focused on the turquoise module. As described in the Methods, we screened the core genes in the turquoise module from two criteria. Both DEAH box protein 9 (DHX9) and ZNF207 met the screening criteria (figure 1E and online supplemental figure S1B-D). DHX9 has already been reported to be involved in immune response mediated by nuclear factor- κ B (NF- κ B)²¹ and regulates toll-like receptor-stimulated immune responses²²; hence, we mainly focused on ZNF207. Taken together, the data show that ZNF207 may be a potential unreported immunosuppressive target.

Furthermore, ZNF207 was observed to be positively correlated with an immune escape signature²³ and negatively correlated with the percentage of infiltrated cytotoxic T cells in HCC tumor tissue (online supplemental figure S1E,F). Elevation of ZNF207 was also observed to correlate with reduced T-cell infiltration in copy number variation analysis (online supplemental figure S1G,H). Moreover, RT-qPCR was performed on 22 clinical HCC samples and revealed strong positive correlations between ZNF207 and CD4 ($R=0.4554$, $p=0.0332$), FOXP3 ($R=0.5198$, $p=0.0132$), CD11b ($R=0.5465$, $p=0.0085$), and CD68 ($R=0.4713$, $p=0.031$). Exceptions were CD8A ($R=-0.4699$, $p=0.0274$), C2 ($R=-0.6148$, $p=0.0023$), and C3 ($R=-0.6126$, $p=0.0024$), which were associated with

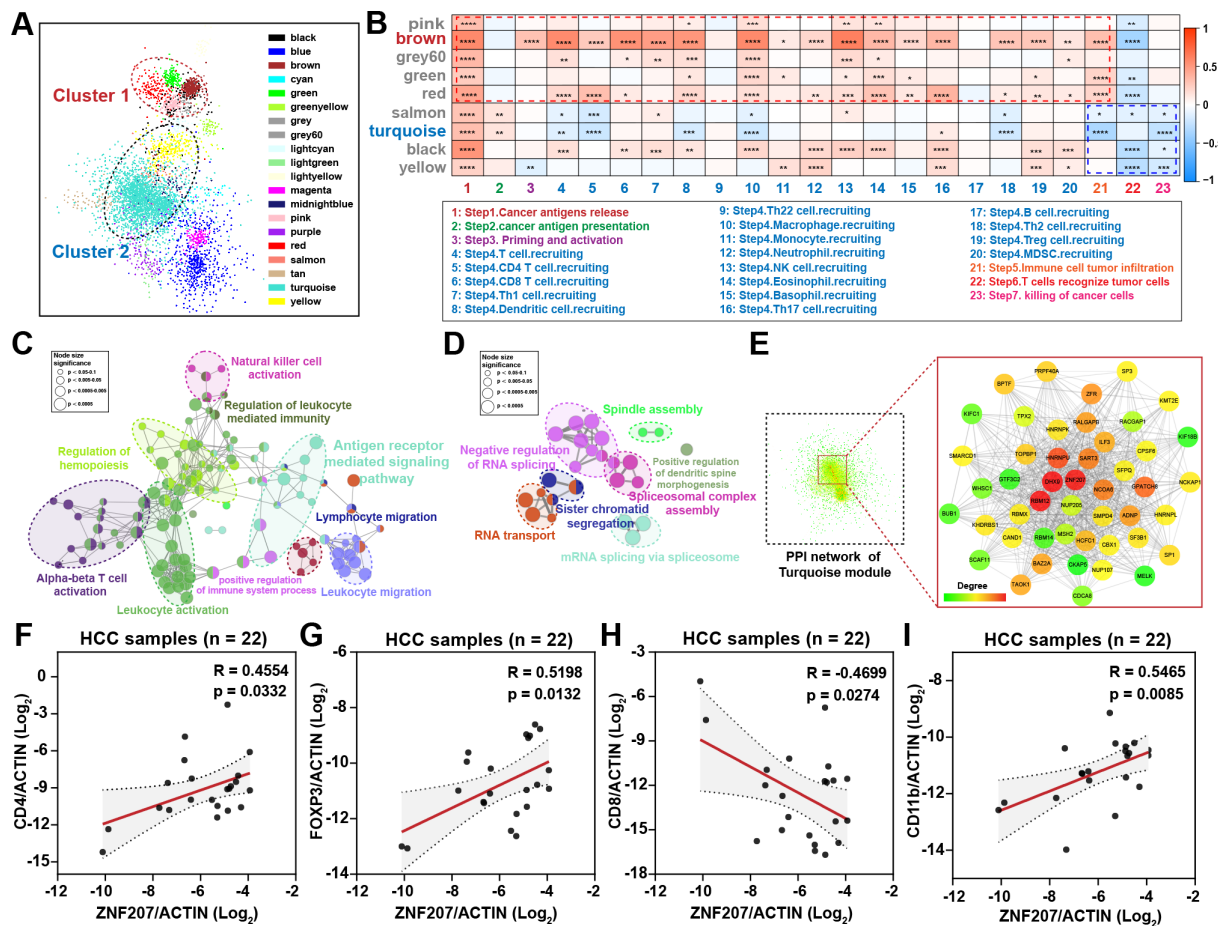


Figure 1 ZNF207 is a potential immunosuppressive target in HCC. (A) Liver cancer data from the TCGA database were used to construct the WGCNA coexpression network; each color represents a type of module, and each node represents a gene. Modules in clusters 1 and 2 show similar expression patterns. (B) Heatmap shows the correlation of each module with cancer immune cycle scores in two clusters. Red represents a positive correlation, while blue represents a negative correlation. The ClueGO plug-in was used to perform pathway enrichment for the core genes in (C) brown and (D) turquoise modules. Each node represents a biological process; nodes with the same color have similar functions. Node size shows the significance of enrichment. (E) PPI network of genes in the turquoise module; the enlarged image shows the core nodes in the network, and the red nodes are the core nodes in the network. (F–I) Clinical HCC samples were used to detect the correlation between immune cell marker genes and *ZNF207* by quantitative reverse transcription PCR (RT-qPCR), $|R| > 0.3$, $n = 22$. * $P < 0.05$; ** $P < 0.01$; *** $P < 0.001$. HCC, hepatocellular carcinoma; MDSC, myeloid-derived suppressor cells; NK, natural killer; PPI, protein–protein interaction; Treg, regulatory T cell; ZNF207, zinc finger protein 207.

cytotoxic T cells and complement immune responses (figure 1F–I and online supplemental figure S1I–K). In summary, through bioinformatics analysis and preliminary experimental verification, we screened and identified *ZNF207* as a potential immunosuppressive target in HCC, which may be correlated with steps of the cancer–immunity cycle (including immune cell infiltration, cancer cell recognition, and killing).

ZNF207 is highly expressed in HCC and associated with poor prognosis

The progression of HCC is usually accompanied by abnormal gene expression and poor prognosis. Expression of *ZNF207* in matched HCC tissues was found to be higher than that in adjacent samples (figure 2A). Data from the Oncomine and GEO databases revealed a consistent trend (figure 2B,C, and online supplemental figure S2A,B). In HCC samples, *ZNF207* showed a significant

increase at both the transcriptional and translational levels (figure 2D,E, and online supplemental figure S2C). Immunohistochemistry (IHC) analysis revealed that *ZNF207* was mainly overexpressed (overexpression (OE)) in the nucleus, consistent with its role as a transcription factor (figure 2F and online supplemental figure S2D). The key genes in HCC progression were usually correlated with cancer stages and patient prognosis. Patients with HCC showed more advanced stage, grade, and T stage in the *ZNF207*^{high} expression group (figure 2G) as well as shorter overall and disease-free survival outcomes in multiple datasets (figure 2H and online supplemental figure S2E,F). Univariate and multivariable Cox model analysis further revealed *ZNF207* as an independent prognostic factor for HCC (online supplemental figure S2G and online supplemental table S1) in online supplemental materials and methods). Overall, our findings

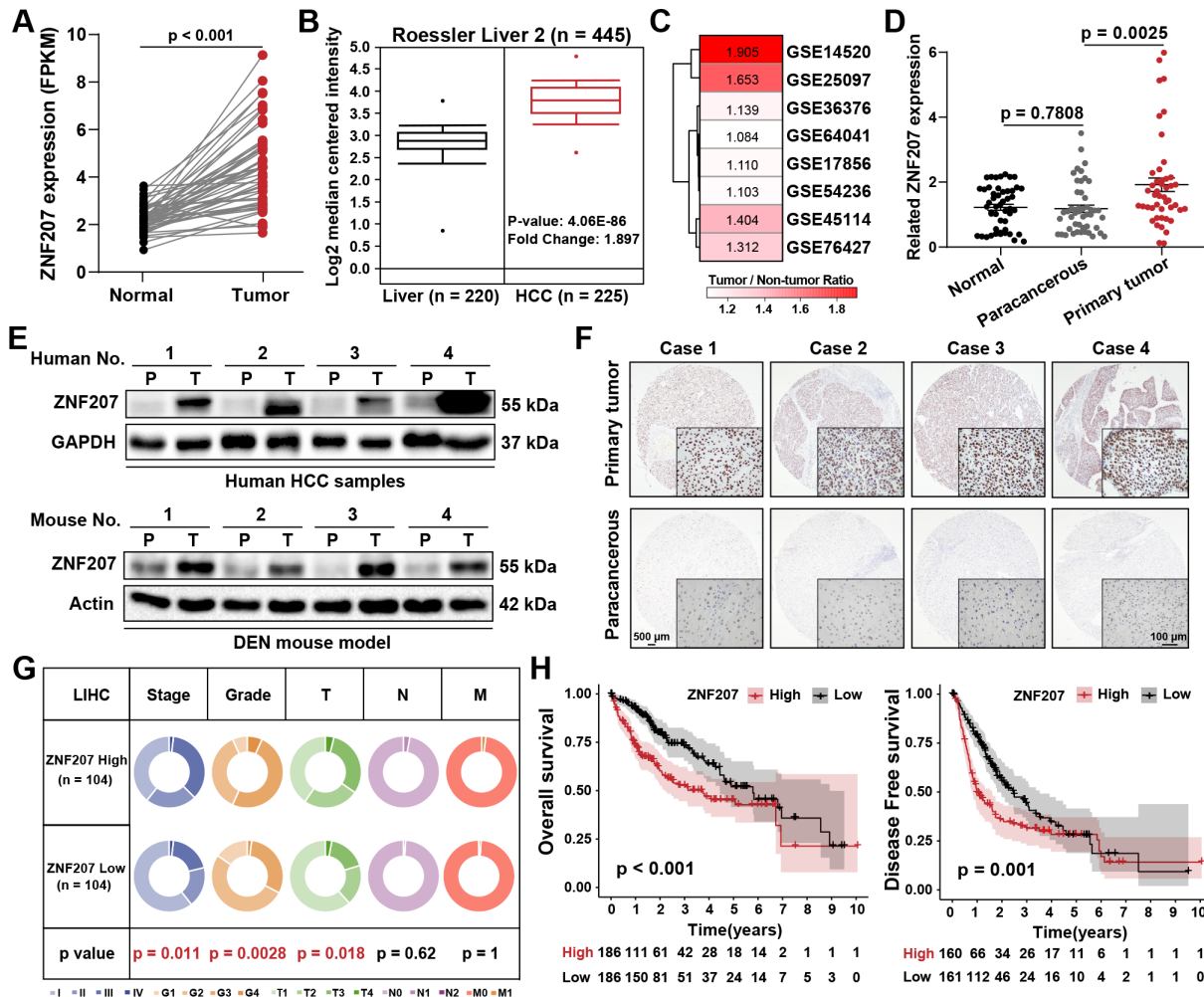


Figure 2 *ZNF207* is highly expressed in HCC and is associated with a poor prognosis. The public databases were used to analyze the differential expression of *ZNF207* in liver cancer and paracancerous tissues. (A) TCGA (n=50), (B) OncoPrint (normal, n=220; tumor, n=225), and (C) GEO databases. (D) RT-qPCR was used to detect the mRNA levels of *ZNF207* in cancer nests (n=50), adjacent tissue (n=50), and normal tissues of patients with HCC (n=49). (E) Western blot was used to measure *ZNF207* protein level in clinical HCC (n=4) and DEN-induced orthotopic HCC samples (n=4). (F) Protein level of *ZNF207* in paracancerous and primary HCC samples was detected by immunohistochemistry (n=30). (G) The circular pie chart shows the proportion difference of clinical indices (including tumor, node, metastasis stages and pathological grade) in the *ZNF207*^{high} and *ZNF207*^{low} expression groups from the TCGA LIHC dataset. (H) Prognostic relationship (OS and DFS) between *ZNF207* and patients with HCC. DEN, diethylnitrosamine; DFS, disease free survival; FPKM, Fragments Per Kilobase of exon model per Million mapped fragments; HCC, hepatocellular carcinoma; OS, overall survival; *ZNF207*, zinc finger protein 207.

show that *ZNF207* is highly expressed in HCC and is associated with a poorer prognosis.

Hypoxia elevates *ZNF207* in HCC

Next, we examined how *ZNF207* was upregulated in HCC by gene set enrichment analysis (GSEA). We found that the 'HYPOXIA_VIA_HIF1A_UP' gene signature was significantly enriched in the *ZNF207*^{high} group (figure 3A). Experimentally, we observed both physically- and chemically-simulated hypoxia could elevate the protein level of *ZNF207* (figure 3B,C, and online supplemental figure S3A), which could be reversed by inhibitors of hypoxia-inducible factor 1 α (HIF1 α) (BAY87-2243) and HIF2 α (PT2385). In comparison, BAY87-2243 exerted a stronger inhibitory effect on *ZNF207* under hypoxia conditions (figure 3D,E). Using plasmids to

overexpress *HIF1 α* and *HIF2 α* under normoxia conditions, we found that the effect of hypoxia on *ZNF207* could be reproduced (figure 3F,G). To analyze the transcriptional regulation effect of HIF on *ZNF207*, we conducted a dual-luciferase reporter gene experiment. Both hypoxia and cobaltous chloride incubation enhanced the fluorescence intensity of the *ZNF207* promoter gene (figure 3H). The ChIP-qPCR assay was used to confirm the candidate HIF binding sites, which could match the consensus sequence 5'-(A/G)CGTG-3'²⁴ in the *ZNF207* promoter. The *ZNF207* promoter (-2000 to +200 from the translation start site (TSS)) region has six HIF consensus-binding sites (figure 3I). Chromatin fragments containing two DNA sequences, located in the promoter region of the *ZNF207* -959/-964 bp relative to

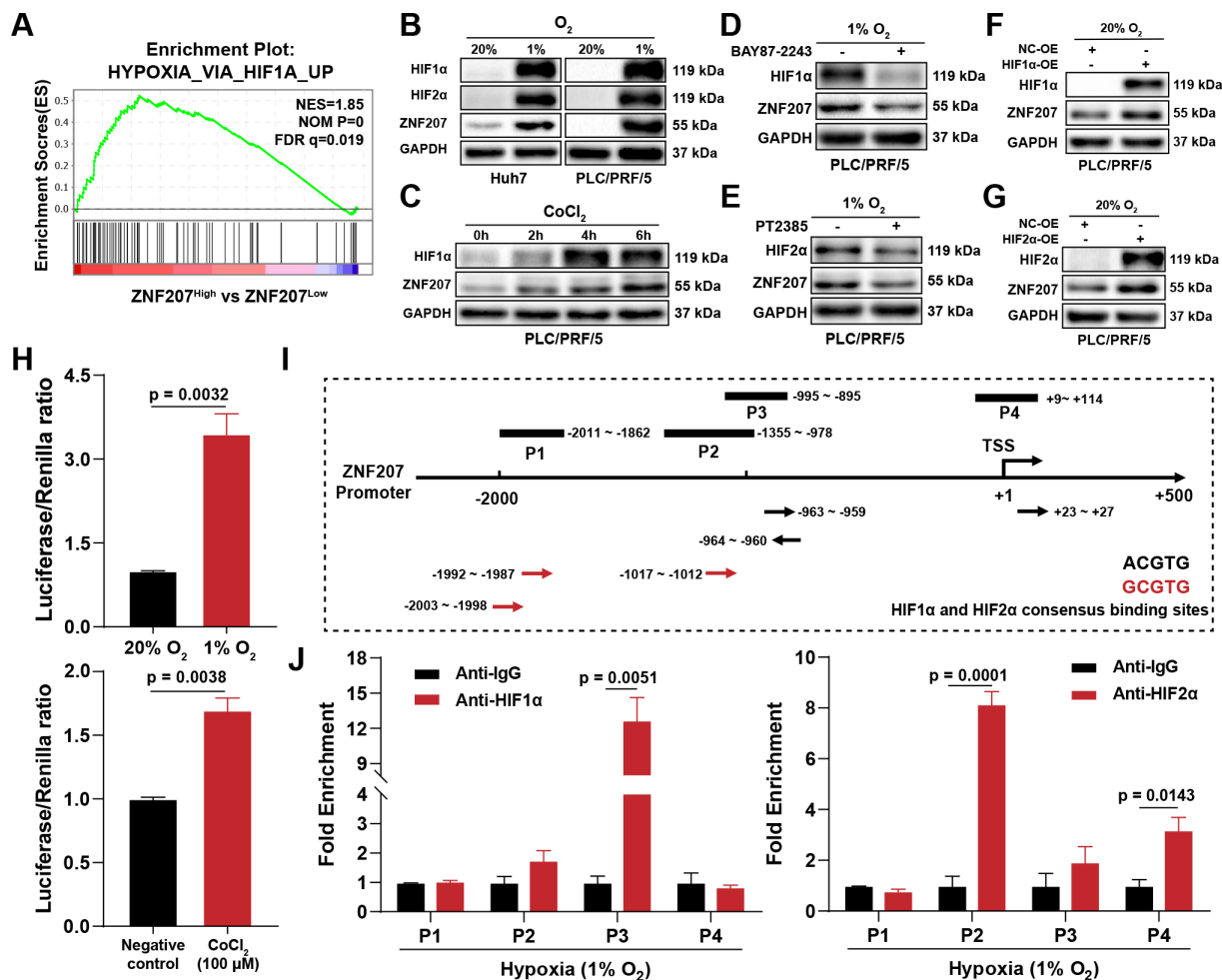


Figure 3 Hypoxia elevates ZNF207 in HCC. (A) HCC gene expression data from the TCGA database were grouped by *ZNF207* expression to perform GSEA analysis; the enrichment plot shows the enriched pathway in the *ZNF207*^{high} expression group. (B) Western blot shows ZNF207, HIF1 α , and HIF2 α protein levels under physical hypoxia in Huh7 and PLC/PRF/5 (1% O₂, 24 hours). (C) PLC/PRF/5 cells treated with 100 μ M CoCl₂ for different periods and detection of ZNF207 protein level. Effects of the (D) HIF1 α inhibitor (BAY87-2243, 10 μ M) and (E) HIF2 α inhibitor (PT2385, 10 μ M) on ZNF207 under hypoxia conditions in PLC/PRF/5 cells. Plasmids were used to overexpress (F) HIF1 α and (G) HIF2 α to observe the changes in ZNF207. (H) Dual-luciferase reporter gene assay was used to evaluate the effect of hypoxia (24 hours) and CoCl₂ (100 μ M) treatment on the *ZNF207* promoter. (I) The transcription binding sites of HIF1 α and HIF2 α in the promoter region of *ZNF207* and the positions of the corresponding primers. (J) Enrichment of HIF1 α and HIF2 α on the *ZNF207* promoter under hypoxia as detected by ChIP-qPCR. CoCl₂, cobaltous chloride; GSEA, gene set enrichment analysis; HCC, hepatocellular carcinoma; ZNF207, zinc finger protein 207.

the TSS, were immunoprecipitated with an anti-HIF-1 α antibody under hypoxia conditions. One DNA sequence located -1012/-1017bp relative to TSS was immunoprecipitated with an anti-HIF2 α antibody under both normoxia and hypoxia conditions (figure 3J and online supplemental figure S3B,C). In brief, hypoxia can elevate *ZNF207* expression in HCC by transcriptional regulation.

ZNF207 promotes HCC associated with CD8⁺ T-cell infiltration and exhaustion

To understand how ZNF207 promotes HCC progression, and whether it is related to tumor immunity, we first evaluated the effect of ZNF207 on cell proliferation in loss-of-function and gain-of-function experiments in vitro. Regardless of *ZNF207*-knockdown (KD) or *ZNF207*-OE, the cell proliferation of HCC cell lines

remained unchanged (online supplemental figure S4A–C). Furthermore, *ZNF207*-KD or *ZNF207*-OE did not alter the growth rate of xenograft tumors in immunodeficient mice (figure 4A,B). These results suggest that *ZNF207* is not crucial for HCC cell proliferation in an immunodeficient microenvironment. Based on previous analysis and experimental results, we hypothesized that hepatoma-intrinsic ZNF207 might promote HCC progression by regulating tumor immunity. *ZNF207*-KD or *ZNF207*-OE Hepa1-6 cells significantly affected tumor growth rate without showing a difference in cell proliferation in vitro (figure 4C,D, and online supplemental figure S4D–F). C57BL/6 mice were subcutaneous inoculated with these cells. *ZNF207*-KD or *ZNF207*-OE changed the positive cell rate of Ki67 and CD31 (online supplemental

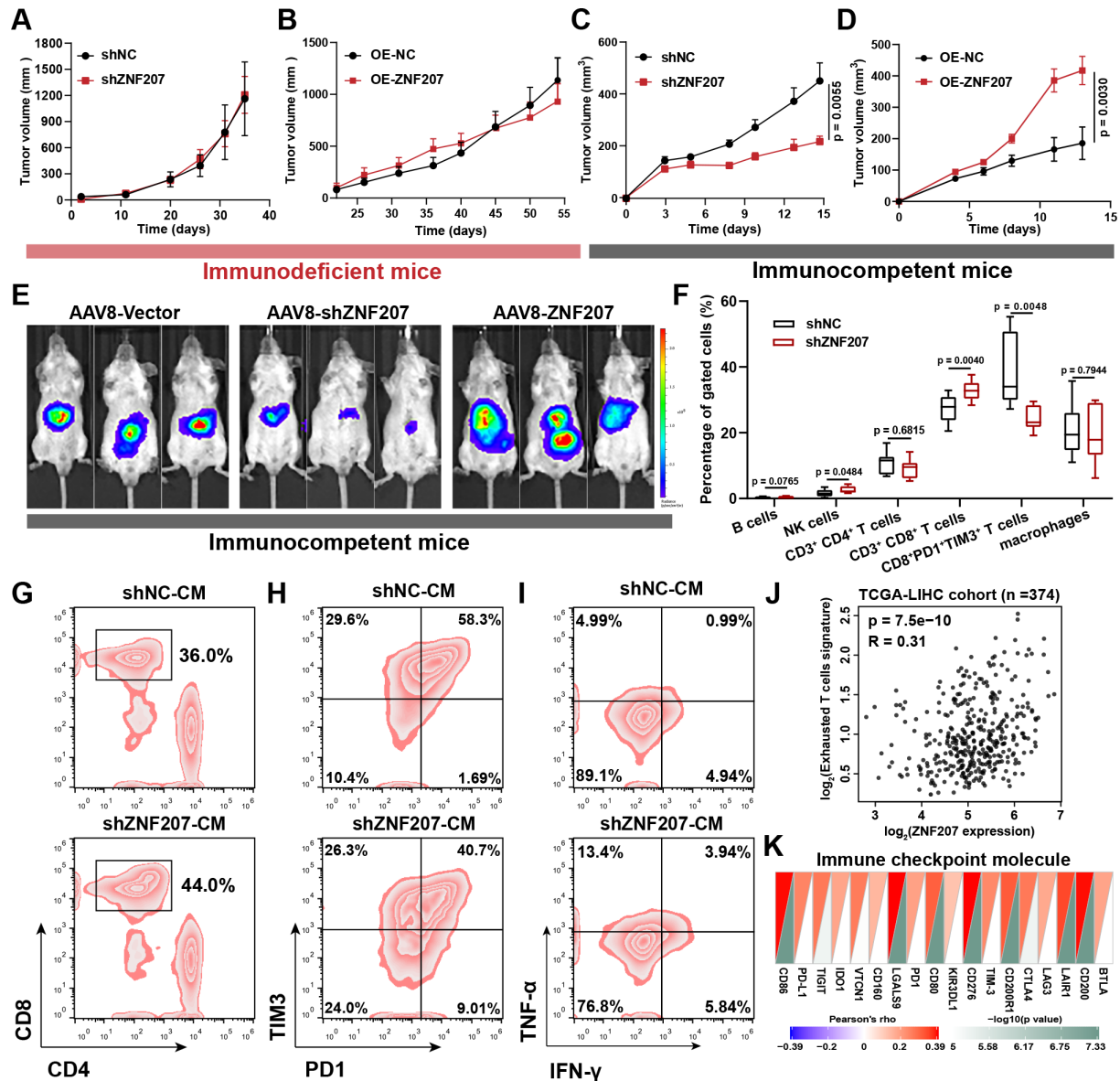


Figure 4 ZNF207 promotes HCC associated with CD8⁺ T-cell infiltration and exhaustion. In vivo xenograft growth curves of (A) *ZNF207*-KD ($n=7$) and (B) *ZNF207*-OE ($n=6$) in HCC cells (HCCLM3 for KD; PLC/PRF/5 for OE) inoculated into immunodeficient BALB/c-nude mice. In vivo xenograft growth curve of (C) *ZNF207*-KD ($n=9$) and (D) *ZNF207*-OE ($n=10$) Hepa1-6 cells in immunocompetent C57BL/6N mice. (E) After 3 days of inoculating H22 cells at the liver capsule of BALB/c mice, *ZNF207*-KD and *ZNF207*-OE adeno-associated virus 8 was injected via the tail vein into mice ($n=8$), and tumor formation was observed by live imaging at the end of the experiment. (F) Flow cytometry was used to find out the difference in immune cell infiltration in *ZNF207*-KD tumors ($n=10$). Conditioned medium from *ZNF207*-KD Hepa1-6 cells used to study its role on CD8⁺ T-cell function, including (G) CD8⁺ T-cell chemotaxis ($n=3$), (H) exhaustion ($n=3$), and (I) IFN- γ ⁺ TNF- α ⁺ CD8⁺ T-cell percentage ($n=3$). (J) Correlation between *ZNF207* and exhausted T-cell signature in the TCGA-LIHC dataset ($n=374$). (K) Correlations heatmap of *ZNF207* and immune checkpoints. HCC, hepatocellular carcinoma; IFN- γ , interferon gamma; KD, knockdown; OE, overexpression; TNF- α , tumor necrosis factor alpha; ZNF207, zinc finger protein 207.

figure S4G–I), two markers often used to evaluate tumor proliferation and angiogenesis. Furthermore, we used adeno-associated virus 8 to intervene on the H22-induced orthotopic model of HCC. *ZNF207*-KD or *ZNF207*-OE adeno-associated virus 8 significantly altered tumor growth in the immunocompetent mice (BALB/c mice) (figure 4E and online supplemental figure S4J). These findings indicate that *ZNF207*-induced HCC progression is associated with tumor immunity.

To clarify how *ZNF207* promotes the progression of HCC through tumor immunity, we performed flow cytometry analysis on *ZNF207*-KD and control tumor tissue. *ZNF207*-KD enhanced CD8⁺ T-cell infiltration and inhibited its exhaustion (figure 4F and online supplemental figure S5A). Moreover, IHC confirmed that the proportion of CD8⁺ T cells was elevated in *ZNF207*-KD tumors (online supplemental figure 5B). Then, the conditioned medium was used to simulate the effect of *ZNF207* on

T-cell function in vitro. The conditioned medium obtained from *ZNF207*-KD Hepa1-6 cells showed no significant chemotactic effects on natural killer cells, B cells, and macrophages, while it exhibited a marked chemotactic effect on CD8⁺ T cells (figure 4G and online supplemental figure S5C-F). Interestingly, the conditioned medium also inhibited the exhaustion of CD8⁺ T cells in vitro (figure 4H and online supplemental figure S5G), which improved its proliferation and cytokine secretion levels (figure 4I and online supplemental figure S5H,I). Interestingly, *ZNF207* is positively correlated with the exhausted T-cell gene signature and immune checkpoint molecules in the TCGA-LIHC dataset, consistent with experimental results (figure 4J,K). The aforementioned

results indicate that *ZNF207* enhances HCC progression through tumor immunity, which is correlated with infiltration and exhaustion of CD8⁺ T cells.

ZNF207 inhibits CD8⁺ T-cell infiltration through the MAPK-CX3CL1 axis

To clarify the potential mechanism by which *ZNF207* affects CD8⁺ T-cell infiltration and exhaustion, we performed RNA sequencing analysis on Hepa1-6-shZNF207 and Hepa1-6-shNC cells (online supplemental figure S6A). GSEA revealed that the immune and metabolic-related signaling pathways were significantly enriched in the *ZNF207*-KD group (figure 5A). Moreover, chemokine, cytokine-cytokine receptor interactions,

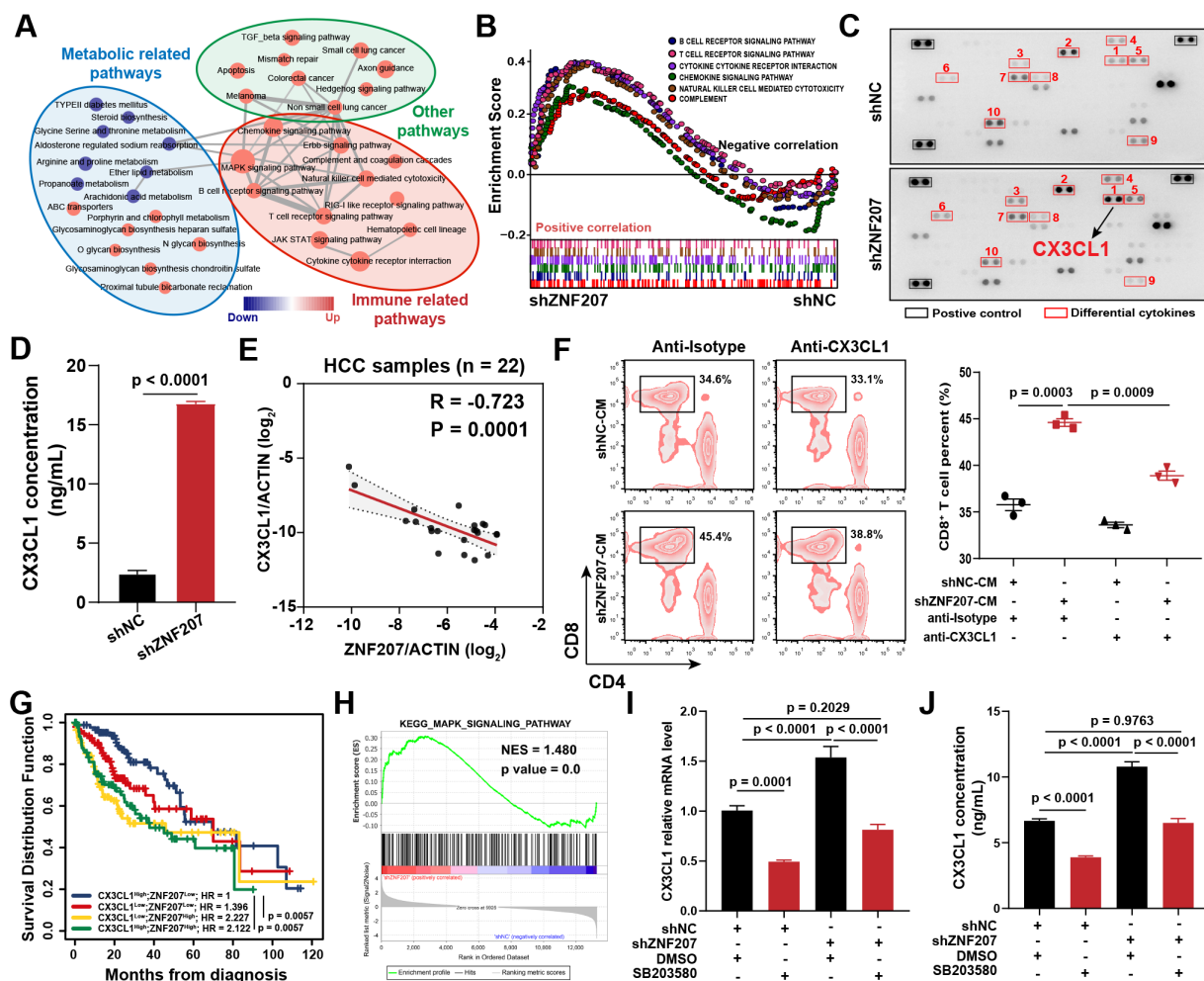


Figure 5 *ZNF207* inhibits CD8⁺ T-cell infiltration through MAPK-CX3CL1 axis. (A) Hepa1-6 knockdown *ZNF207* cells were used for RNA sequencing and then subjected to GSEA. Three major types of signal pathways are significantly enriched. (B) GSEA diagram of immune-related signaling pathways significantly upregulated in the *ZNF207*-KD group. (C) Cytokine array was used to detect 111 cytokines in the CM of *ZNF207*-KD Hepa1-6 cells; cytokines that significantly changed are boxed in red. (D) Concentration of CX3CL1 in the *ZNF207*-KD CM was determined by ELISA ($n=4$). (E) Scatter plot shows the correlation between *ZNF207* and CX3CL1 in 22 HCC samples, $|R|>0.3$; $p<0.05$ represents a significant correlation ($n=22$). (F) The T-cell migration experiment was used to study the chemotaxis of CM from *ZNF207*-KD Hepa1-6 cells, and CX3CL1 neutralizing antibody was further added to observe the changes in T-cell migration ($n=3$). (G) Combination survival analysis based on CX3CL1 and *ZNF207* expressions using the TCGA-LIHC dataset. (H) GSEA map of MAPK signaling pathway enriched in Hepa1-6 shZNF207 group. (I) gene expression of CX3CL1 after p38 MAPK inhibitor SB203580 (10 μ M) treatment in Hepa1-6 for 48 hours ($n=6$). (J) concentration of CX3CL1 in Hepa1-6-shZNF207 cell medium after treatment with p38 MAPK inhibitor SB203580 (10 μ M) for 48 hours ($n=4$). CM, conditioned medium; CX3CL1, C-X3-C-motif ligand; GSEA, gene set enrichment analysis; HCC, hepatocellular carcinoma; KD, knockdown; *ZNF207*, zinc finger protein 207.

and T-cell receptor signaling pathways were upregulated (figure 5B and online supplemental figure S6B). Subsequently, we verified the upregulation of genes in immune-related pathways by RT-qPCR (online supplemental figure S6C). The upregulation of multiple cytokines and chemokines suggests that ZNF207 may change T-cell functions by influencing cytokine secretion; therefore, we performed a cytokine array to compare 111 cytokines in the cell supernatant and lysate of Hepa1-6-shZNF207 and Hepa1-6-shNC cells. Several cytokines were reportedly closely related to T-cell chemotaxis, such as CX3CL1, CXCL1, CXCL10, and CXCL16, which were significantly increased. Specifically, we mainly focused on CX3CL1 because it had a consistent trend in the supernatant and lysate (figure 5C and online supplemental figure S6D-F). Subsequently, we confirmed the upregulation of CX3CL1 in cell supernatant by ELISA (figure 5D). Furthermore, strong negative correlations between ZNF207 and CX3CL1 were observed in human HCC samples (figure 5E). Next, we determined whether ZNF207-KD-induced CX3CL1 secretion is critical for CD8⁺ T cell chemotaxis. When treated with CX3CL1 neutralizers, the chemotactic effect of the conditioned medium on CD8⁺ T cells was weakened (figure 5F). Combination survival analysis also revealed that patients in the CX3CL1^{low}ZNF207^{high} group had the worst overall survival (OS) and highest HR, while the CX3CL1^{high}ZNF207^{low} group showed the best survival outcomes (figure 5G). These findings suggest that CX3CL1 plays an important role in ZNF207-mediated CD8⁺ T-cell infiltration and HCC progression.

Previous research has shown that p38 MAPK can regulate CX3CL1 expression in human astrocytes and smooth muscle cells.^{25, 26} Therefore, we hypothesized that a similar regulatory mechanism might exist in HCC cells. In agreement, the MAPK signaling pathway was significantly enriched in the ZNF207-KD group (figure 5A,H). Moreover, we verified the core genes in the MAPK pathway by RT-qPCR, which all showed an increased expression (online supplemental figure S6I,J). We also proved that the p38 MAPK inhibitor (SB203580) can directly inhibit CX3CL1 in Hepa1-6 cells, and the overexpression of CX3CL1 by ZNF207-KD can also be reversed by SB203580 (figure 5I,J). In brief, we showed that ZNF207 might inhibit CD8⁺ T-cell infiltration through the MAPK-CX3CL1 axis.

ZNF207 promotes CD8⁺ T-cell exhaustion by increasing kynurenine level

As previous results showed (figure 5A), apart from immune pathways, multiple metabolic pathways (mainly amino acid metabolism pathways) were significantly enriched (figure 5A and online supplemental figure S7A). Various studies have reported the influence of metabolites on T-cell function; thus, we hypothesized that ZNF207 may affect tumor metabolism in regulating CD8⁺ T-cell function. Therefore, we performed metabolomic analysis on Hepa1-6-shZNF207 versus Hepa1-6-shNC cells. Consistent with the pathway enrichment results, various metabolites were downregulated

after ZNF207-KD, with amino acids being the largest components of the differential metabolites (figure 6A and online supplemental figure S7B,C). The Kyoto Encyclopedia of Genes and Genomes pathway enrichment analysis revealed that differential metabolites were significantly enriched in the tryptophan metabolism pathway. The metabolite levels in the tryptophan metabolism pathway, including that of kynurenine, were significantly suppressed after ZNF207-KD (figure 6B). As expected, ZNF207-KD suppressed kynurenine levels in cell supernatants while increasing in stable ZNF207 expression (figure 6C). Multiple studies have shown that kynurenine released by tumor cells can induce T-cell exhaustion,²⁷⁻³⁰ which explains a partial mechanism of how ZNF207 promotes CD8⁺ T-cell exhaustion in HCC. Moreover, we added kynurenine to the conditioned medium of ZNF207-KD cells to monitor CD8⁺ T-cell exhaustion. Indeed, kynurenine supplementation significantly induced CD8⁺ T-cell exhaustion (figure 6D and online supplemental figure S7D). Taken together, these data show that kynurenine is involved in the CD8⁺ T-cell exhaustion mediated by ZNF207.

ZNF207 transcriptionally regulates IDO1 to promote kynurenine production

To understand how ZNF207 changes kynurenine metabolism, we focused on the key genes in the kynurenine metabolic pathway, which were significantly downregulated in the ZNF207-KD group (online supplemental figure S7E). ZNF207 expression only elevated the mRNA levels of IDO1, but not IDO2 or TDO2 (online supplemental figure S7F,G). Based on these findings, we hypothesize that ZNF207 can transcriptionally regulate IDO1. We used a dual fluorescein reporter gene experiment to investigate this conjecture, which showed an increased fluorescence intensity when the IDO1 promoter-luciferase plasmid was cotransfected with ZNF207-OE plasmid (figure 6E). ChIP-qPCR confirmed that ZNF207 could bind to three regions (-1213→-1028bp, -1143→-976bp, and -1040→-898bp relative to TSS) of the IDO1 promoter (figure 6F). Inhibition of IDO1 with a specific inhibitor PF-06840003 reversed kynurenine levels mediated by ZNF207 expression (figure 6G). In addition, PF-06840003 treatment reversed CD8⁺ T-cell exhaustion caused by the conditioned medium from the ZNF207-OE cell line (figure 6H and online supplemental figure S7H). The in vivo experiment showed that PF-06840003 treatment reversed the tumor growth-promoting effect of ZNF207-OE, reflecting the key role of the IDO1 pathway in ZNF207-mediated HCC growth (online supplemental figure S7I). In summary, our work preliminary proved that ZNF207 can transcriptionally regulate IDO1 to elevate kynurenine and induce CD8⁺ T-cell exhaustion.

ZNF207 is a potential therapeutic target in combination with anti-PD1 therapy

In this study, we found that ZNF207 could promote HCC progression by regulating tumor immunity. Therefore, we further investigated the potential of ZNF207 as a therapeutic target in combination with anti-PD1 therapy in patients with HCC. Although anti-PD1 treatment alone

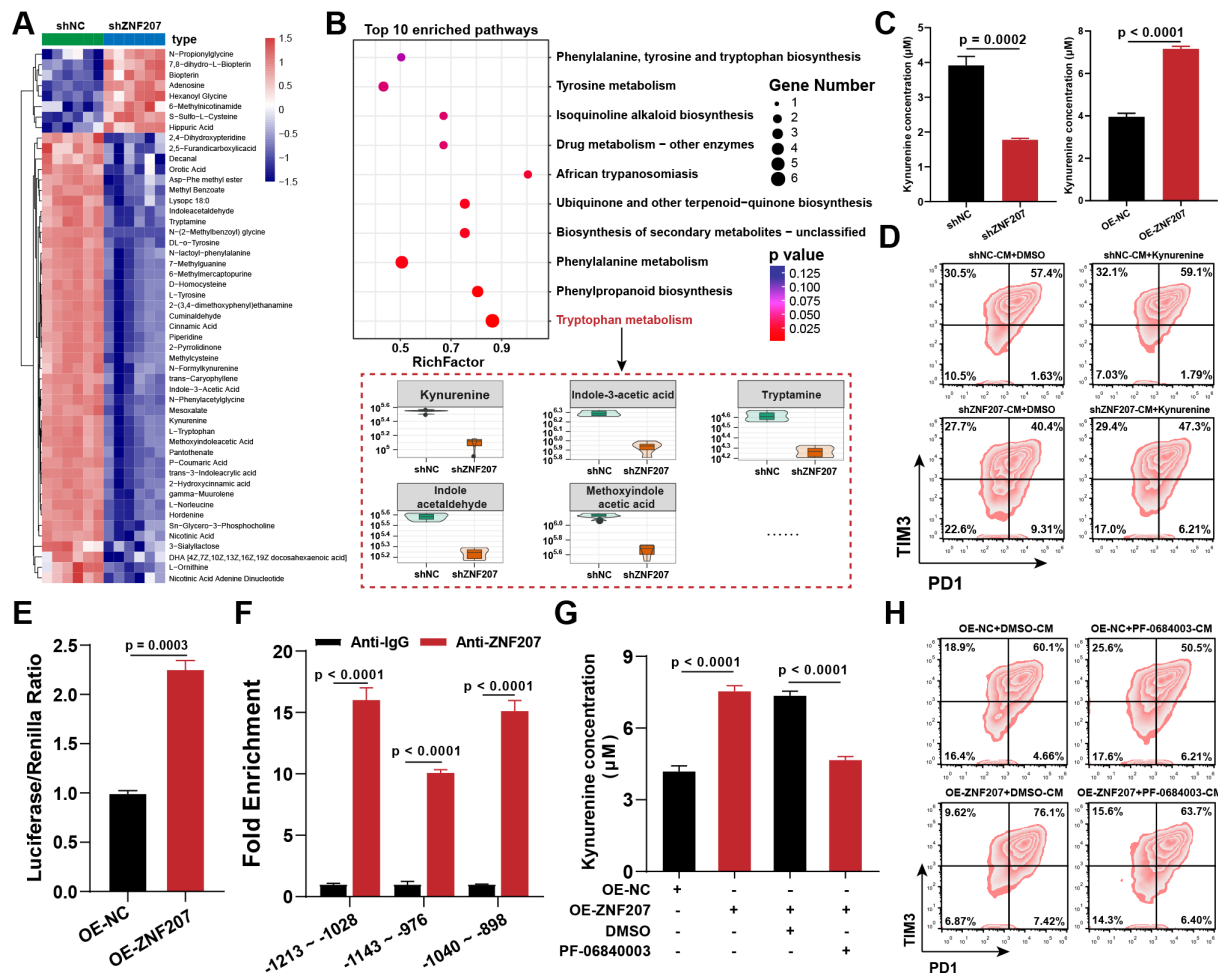


Figure 6 ZNF207 promotes CD8⁺ T-cell exhaustion by increasing kynurenine levels. (A) Heatmap of differential metabolites after ZNF207-KD, red represents elevated metabolites and blue represents decreased metabolites. (B) KEGG pathway analysis of differential metabolites after *ZNF207*-KD (top) and levels of enriched metabolites in tryptophan metabolism pathway (bottom). (C) Concentration of kynurenine in the CM of *ZNF207*-KD and *ZNF207*-OE cells (n=4). (D) Flow cytometry was used to detect the effect of Hepa1-6-sh*ZNF207*-CM supplemented with kynurenine on CD8⁺ T-cell exhaustion; PD1 and Tim3 double-positive cells are defined as exhausted T cells (n=3). (E) The dual-luciferase reporter gene experiment was used to study the transcriptional regulation of *IDO1* by *ZNF207*. Luciferase levels of the *IDO1* promoter were detected after cotransfection of the *ZNF207*-OE plasmid and *IDO1* promoter plasmid (n=3). (F) Enrichment of *ZNF207* at the *IDO1* promoter region of PLC/PRF/5 after *ZNF207*-OE, as determined by ChIP-qPCR (n=4). (G) Concentration of kynurenine in the cell supernatant after treatment with *IDO1* inhibitor PF-06840003 (2 μM) for 6 hours (n=4). (H) CD8⁺ T cells were treated with the CM from *ZNF207*-OE cells pretreated with DMSO and PF-06840003 (2 μM) for 48 hours; T-cell exhaustion was subsequently monitored by flow cytometry. CM, conditioned medium; DMSO, dimethyl sulfoxide; *IDO1*, indoleamine 2,3-dioxygenase 1; KEGG, Kyoto Encyclopedia of Genes and Genomes; OE, overexpression; *ZNF207*, zinc finger protein 207.

could inhibit tumor growth, *ZNF207*-KD combined with PD1 monoclonal antibody exhibited an outstanding tumor suppression effect (figure 7A–C and online supplemental figure S8A). The percentage of PCNA-positive cells in the *ZNF207*-KD plus anti-PD1 treatment group was the lowest, while infiltrating T cells were increased significantly (figure 7D). To further study the value of *ZNF207* in predicting immunotherapy responsiveness, we used Tumor Immune Dysfunction and Exclusion (TIDE) and Submap algorithms as previously reported to predict the immunotherapeutic response rate of patients with different *ZNF207* expressions from the TCGA-LIHC dataset^{31 32} (figure 7E). Only 21.6% of patients in the *ZNF207*^{high} expression group responded to

immunotherapy compared with 70.3% in the *ZNF207*^{low} group (figure 7F). In addition, patients in the *ZNF207*^{low} expression group exhibited a better response to PD1 monoclonal antibody treatment than the CTLA-4 monoclonal antibody (figure 7G). Next, we also evaluated the prognostic value of *ZNF207* for immune-checkpoint therapy by assigning patients into either high or low *ZNF207* groups in two PD1 antibody-treated cohorts. Patients in the *ZNF207*^{low} expression group exhibited prolonged survival outcomes (online supplemental figure S8B–E). Receiver operating characteristic curve (ROC) analyses of the GSE78220 cohorts (PD1-treated cohort) revealed *ZNF207* as a predictive biomarker for the efficacy of anti-PD1 therapy (online supplemental

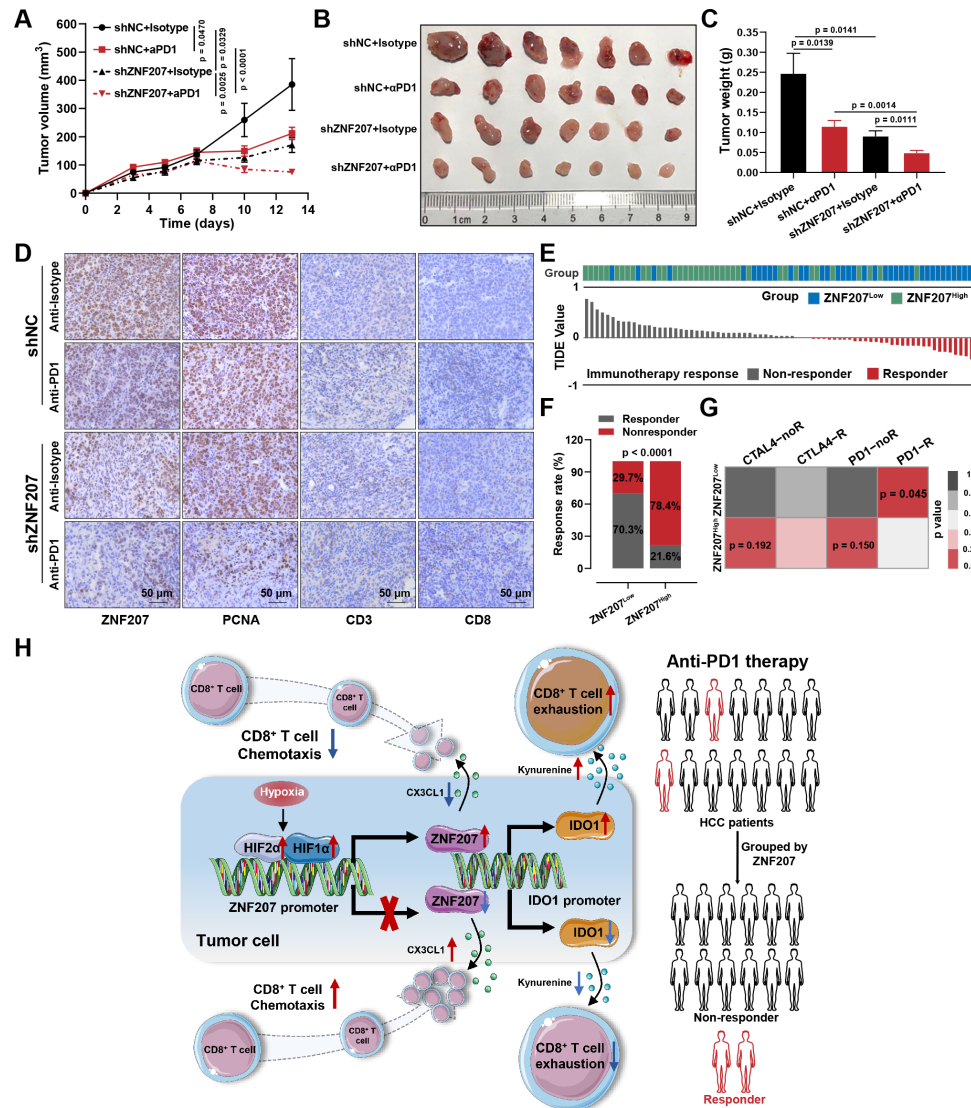


Figure 7 ZNF207 is a potential combination target for anti-PD1 therapy. (A) In vivo Hepa1–6 xenograft tumor growth curves of ZNF207-knockdown combined with PD1 treatment (n=7). (B) Image of the xenograft tumor at the end of the experiment (n=7). (C) Tumor weight statistic results of each group (n=7). (D) Immunohistochemistry was used to detect protein levels of ZNF207, PCNA, CD3, and CD8 in each group. (E) TIDE algorithm was used to predict the immunotherapeutic responses of patients with HCC in different ZNF207 expression groups. The histogram shows the TIDE score of each sample; gray represents patients who are not responsive to immunotherapy, and red represents patients who are responsive to immunotherapy. (F) Rates of response to immunotherapy in ZNF207^{high} and ZNF207^{low} expression groups. (G) Effects of CTLA4 and PD1 monoclonal antibody on patients with HCC in different ZNF207 expression groups. (H) Schematic diagram of how ZNF207 regulates tumor immunity and promotes HCC progression. HCC, hepatocellular carcinoma; PD1, programmed cell death protein 1; ZNF207, zinc finger protein 207.

figure S8F). Taken together, our findings suggested that ZNF207 can be a biomarker and therapeutic target in combination with anti-PD1 therapy for HCC.

DISCUSSION

Understanding the process of tumor immunity is crucial for screening immunosuppressive targets in cancers. We used the cancer–immunity cycle score to quantify immune cycle processes with combined WGCNA and system analysis to identify ZNF207 as an immunosuppressive target in HCC. However, ZNF207 has been reported to be highly expressed in HCC, the mechanism by

which ZNF207 accelerates HCC progression remained unknown.¹⁷ Compared with previously discovered functions,^{15 16 33} we reported its immunosuppressive function for the first time. Our in vivo animal experiment showed that ZNF207-KD combined with anti-PD1 therapy has strong therapeutic potential in HCC.

Insufficient T-cell infiltration may explain why some patients do not respond to immunotherapy.^{34–36} ZNF207 inhibition elevated the level of various chemokines and cytokines, such as CX3CL1, CXCL1, CXCL10, and CXCL16, which could promote T-cell chemotaxis. In our study, we showed that ZNF207 could inhibit CX3CL1

secretion via p38 MAPK. However, the direct effectors by which ZNF207 regulates p38 MAPK signaling still need to be elucidated in the future. In addition to CX3CL1, many other cytokines and chemokines may also play important roles in CD8⁺ T-cell migration. For instance, CXCL5, which inhibits chimeric antigen receptor T-cell infiltration into tumor tissues is reportedly significantly decreased after ZNF207-KD.^{37,38} Furthermore, vascular endothelial growth factor, an important angiogenesis factor that not only promotes tumor angiogenesis but also inhibits T-cell functions,^{39–41} was found to be suppressed in the ZNF207-KD group (online supplemental figure 6G) and showed a positive correlation with ZNF207 (online supplemental figure 6H). These findings suggest that ZNF207 can inhibit T-cell infiltration by altering chemokine levels.

In addition to inhibiting CD8⁺ T-cell infiltration, ZNF207 can also promote T-cell exhaustion. Mechanistically, ZNF207 silencing inhibits IDO1 transcription and kynurenine synthesis—key metabolites in tryptophan signaling reported to speed up T-cell exhaustion.^{27–29,42} PF-06840003, an IDO1 inhibitor, reversed CD8⁺ T-cell exhaustion mediated by condition medium from the ZNF207-overexpressed cell line. These data suggest that ZNF207 changes tumor immunity by affecting T-cell function. In the open-label phase I/II trial, epacadostat (a potent and highly selective IDO1 enzyme inhibitor) plus pembrolizumab in patients with advanced solid tumors was well tolerated and had encouraging anti-tumor activity.⁴³ However, in a phase III, randomized, double-blind study, epacadostat plus pembrolizumab did not improve progression-free survival or OS in patients with unresectable or metastatic melanoma.⁴⁴ The internal mechanism of the IDO1 inhibitor and PD1 monoclonal antibody is similar—both inhibit T-cell exhaustion—but this did not resolve the problem of T-cell infiltration. We hypothesize that despite CD8⁺ T-cell exhaustion decreasing after PD1 therapy or IDO1 inhibition, the T-cell infiltration is still insufficient. Therefore, it is quite difficult for T cells to inhibit tumor progression. In our study, the combination of inhibiting ZNF207 and PD1 monoclonal antibody treatment showed a strong anti-tumor effect. We posit that when compared with IDO1 inhibitors, inhibiting ZNF207 not only inhibits CD8⁺ T-cell exhaustion but also promotes T-cell infiltration through multiple cytokines. Therefore, the development of small-molecule drugs targeting ZNF207 has great potential as a combination therapy with anti-PD1.

The current research also has its limitations. For example, the xenograft tumor model cannot simulate the microenvironment of the orthotopic tumor well. In addition, we used the TIDE and Submap algorithms to predict the response of patients with HCC for the efficacy of immune checkpoint inhibitors by ZNF207 expression. However, this theoretical proof still needs to be tested in a clinical setting.

Figure 7H shows how hypoxia can transcriptionally elevate ZNF207 by HIF proteins. In conclusion, inhibiting

ZNF207 enhanced CX3CL1-induced chemotaxis of CD8⁺ T cells into tumor tissues. In addition, silencing ZNF207 reduced kynurenine synthesis by suppressing transcriptional regulation of IDO1, which in turn reversed CD8⁺ T-cell exhaustion, thereby reshaping the tumor microenvironment. ZNF207 can be considered a potential biomarker and combination target for anti-PD1 therapy in HCC. The development of small-molecule drugs targeting ZNF207 may provide new possibilities for PD1 monoclonal antibody combination therapy.

Acknowledgements We kindly express our appreciation to Xiao Ya Hua Tu for the R scripts related to bioinformatics analysis. We are grateful to Yumeng Shen (Public Platform of State Key Laboratory of Natural Medicines) and Xicheng Chen (Public Experimental Platform of Nanjing Medical University) for their assistance with the flow cytometry analysis. The Home for Researchers editorial team (www.home-for-researchers.com) provided the language editing services.

Contributors XW and YY developed the study concept and design. XW, TZ, XC, YW, XT and HT interpreted and analyzed the data. XW, TZ, XC, YD, HT, YW, SG, and HW performed the experiments. XW, TZ, and XT wrote the manuscript. All authors approved the final version of the manuscript. YY accepts full responsibility for the work and/or the conduct of the study, had access to the data, and controlled the decision to publish.

Funding This study was funded by the National Key New Drug Innovation Program, the Ministry of Science and Technology of China (No: 2018ZX09201017-006), the National Natural Science Foundation of China (82104219, 82003812), the Natural Science Foundation of Jiangsu Province (number BK20180575), the Fundamental Research Funds for the Central Universities (2632022ZD04), and the Outstanding Talents Research Startup Fund of Xuzhou Medical University (D2021049).

Competing interests There are no competing interests.

Patient consent for publication Not applicable.

Ethics approval Ethical approval for animal experiments in this study was obtained from the Center for New Drug Evaluation and Research, China Pharmaceutical University (Nanjing, China), and all procedures were done in accordance with the National Institutes of Health Guide for the Care and Use of Laboratory Animals.

Provenance and peer review Not commissioned; externally peer reviewed.

Data availability statement Data are available in a public, open access repository. All data used or analyzed are included in this article and are available from the corresponding author upon reasonable request. The RNA sequencing data in this manuscript have been deposited in NCBI's Gene Expression Omnibus and are accessible using accession number GSE167935.

Supplemental material This content has been supplied by the author(s). It has not been vetted by BMJ Publishing Group Limited (BMJ) and may not have been peer-reviewed. Any opinions or recommendations discussed are solely those of the author(s) and are not endorsed by BMJ. BMJ disclaims all liability and responsibility arising from any reliance placed on the content. Where the content includes any translated material, BMJ does not warrant the accuracy and reliability of the translations (including but not limited to local regulations, clinical guidelines, terminology, drug names and drug dosages), and is not responsible for any error and/or omissions arising from translation and adaptation or otherwise.

Open access This is an open access article distributed in accordance with the Creative Commons Attribution Non Commercial (CC BY-NC 4.0) license, which permits others to distribute, remix, adapt, build upon this work non-commercially, and license their derivative works on different terms, provided the original work is properly cited, appropriate credit is given, any changes made indicated, and the use is non-commercial. See <http://creativecommons.org/licenses/by-nc/4.0/>.

ORCID iD

Yong Yang <http://orcid.org/0000-0002-2841-8420>

REFERENCES

- Hu W, Zheng S, Guo H, et al. PLAGL2-EGFR-HIF-1/2 α signaling loop promotes HCC progression and erlotinib insensitivity. *Hepatology* 2021;73:674–691.

- 2 Finn RS, Ryoo B-Y, Merle P, *et al.* Pembrolizumab as second-line therapy in patients with advanced hepatocellular carcinoma in KEYNOTE-240: a randomized, double-blind, phase III trial. *J Clin Oncol* 2020;38:193–202.
- 3 Iñarrairaegui M, Melero I, Sangro B. Immunotherapy of hepatocellular carcinoma: facts and hopes. *Clin Cancer Res* 2018;24:1518–24.
- 4 Ruf B, Heinrich B, Greten TF. Immunobiology and immunotherapy of HCC: spotlight on innate and innate-like immune cells. *Cell Mol Immunol* 2021;18:112–27.
- 5 Wang X, Li B, Kim YJ, *et al.* Targeting monoamine oxidase A for T cell-based cancer immunotherapy. *Sci Immunol* 2021;6. doi:10.1126/sciimmunol.abh2383. [Epub ahead of print: 14 05 2021].
- 6 Zarour HM. Reversing T-cell dysfunction and exhaustion in cancer. *Clin Cancer Res* 2016;22:1856–64.
- 7 Zappasodi R, Merghoub T, Wolchok JD. Emerging concepts for immune checkpoint Blockade-Based combination therapies. *Cancer Cell* 2018;34:690.
- 8 Zou W, Wolchok JD, Chen L. Pd-L1 (B7-H1) and PD-1 pathway blockade for cancer therapy: mechanisms, response biomarkers, and combinations. *Sci Transl Med* 2016;8:328rv4.
- 9 Greten TF, Lai CW, Li G, *et al.* Targeted and immune-based therapies for hepatocellular carcinoma. *Gastroenterology* 2019;156:510–24.
- 10 Finn RS, Qin S, Ikeda M, *et al.* Atezolizumab plus bevacizumab in unresectable hepatocellular carcinoma. *N Engl J Med* 2020;382:1894–905.
- 11 Kudo M. Combination cancer immunotherapy with molecular targeted Agents/Anti-CTLA-4 antibody for hepatocellular carcinoma. *Liver Cancer* 2019;8:1–11.
- 12 Chen DS, Mellman I. Oncology meets immunology: the cancer-immunity cycle. *Immunity* 2013;39:1–10.
- 13 Hu Y, Sun H, Zhang H, *et al.* An Immunogram for an individualized assessment of the antitumor immune response in patients with hepatocellular carcinoma. *Front Oncol* 2020;10:1189.
- 14 Jiang H, He X, Wang S, *et al.* A microtubule-associated zinc finger protein, BuGZ, regulates mitotic chromosome alignment by ensuring Bub3 stability and kinetochore targeting. *Dev Cell* 2014;28:268–81.
- 15 Fang F, Xia N, Angulo B, *et al.* A distinct isoform of ZNF207 controls self-renewal and pluripotency of human embryonic stem cells. *Nat Commun* 2018;9:4384.
- 16 Pahl PM, Hodges YK, Meltesen L, *et al.* ZNF207, a ubiquitously expressed zinc finger gene on chromosome 6p21.3. *Genomics* 1998;53:410–2.
- 17 Zhou C, Li N. [Expression of ZNF207 in hepatocellular carcinoma and its significance]. *Zhong Nan Da Xue Xue Bao Yi Xue Ban* 2019;44:406–12.
- 18 Wang W, Yang X, Dai J, *et al.* Prostate cancer promotes a vicious cycle of bone metastasis progression through inducing osteocytes to secrete GDF15 that stimulates prostate cancer growth and invasion. *Oncogene* 2019;38:4540–59.
- 19 Howley BV, Link LA, Grelet S, *et al.* A CREB3-regulated ER-Golgi trafficking signature promotes metastatic progression in breast cancer. *Oncogene* 2018;37:1308–25.
- 20 Frankiw L, Baltimore D, Li G. Alternative mRNA splicing in cancer immunotherapy. *Nat Rev Immunol* 2019;19:675–87.
- 21 Ng YC, Chung W-C, Kang H-R, *et al.* A DNA-sensing-independent role of a nuclear RNA helicase, DHX9, in stimulation of NF- κ B-mediated innate immunity against DNA virus infection. *Nucleic Acids Res* 2018;46:9011–26.
- 22 Dempsey A, Keating SE, Carty M, *et al.* Poxviral protein E3-altered cytokine production reveals that DExD/H-box helicase 9 controls Toll-like receptor-stimulated immune responses. *J Biol Chem* 2018;293:14989–5001.
- 23 Lawson KA, Sousa CM, Zhang X, *et al.* Functional genomic landscape of cancer-intrinsic evasion of killing by T cells. *Nature* 2020;586:120–6.
- 24 Semenza GL, Jiang BH, Leung SW, *et al.* Hypoxia response elements in the aldolase A, enolase 1, and lactate dehydrogenase a gene promoters contain essential binding sites for hypoxia-inducible factor 1. *J Biol Chem* 1996;271:32529–37.
- 25 Gan A-M, Butoi ED, Manea A, *et al.* Inflammatory effects of resistin on human smooth muscle cells: up-regulation of fractalkine and its receptor, CX3CR1 expression by TLR4 and Gi-protein pathways. *Cell Tissue Res* 2013;351:161–74.
- 26 Sheng WS, Hu S, Ni HT, *et al.* Win55,212-2 inhibits production of CX3CL1 by human astrocytes: involvement of p38 MAP kinase. *J Neuroimmunol Pharmacol* 2009;4:244–8.
- 27 Rad Pour S, Morikawa H, Kiani NA, *et al.* Exhaustion of CD4+ T-cells mediated by the kynurenine pathway in melanoma. *Sci Rep* 2019;9:12150.
- 28 Liu Y, Liang X, Dong W, *et al.* Tumor-Repopulating Cells Induce PD-1 Expression in CD8+ T Cells by Transferring Kynurenine and AhR Activation. *Cancer Cell* 2018;33:480–94.
- 29 Mezrich JD, Fehner JH, Zhang X, *et al.* An interaction between kynurenine and the aryl hydrocarbon receptor can generate regulatory T cells. *J Immunol* 2010;185:3190–8.
- 30 Jonescheitl H, Oberg H-H, Gonnermann D, *et al.* Influence of Indoleamine-2,3-Dioxygenase and its metabolite kynurenine on $\gamma\delta$ T cell cytotoxicity against ductal pancreatic adenocarcinoma cells. *Cells* 2020;9. doi:10.3390/cells9051140. [Epub ahead of print: 06 05 2020].
- 31 Hoshida Y, Brunet J-P, Tamayo P, *et al.* Subclass mapping: identifying common subtypes in independent disease data sets. *PLoS One* 2007;2:e1195.
- 32 Jiang P, Gu S, Pan D, *et al.* Signatures of T cell dysfunction and exclusion predict cancer immunotherapy response. *Nat Med* 2018;24:1550–8.
- 33 Liu C, Banister CE, Buckhaults PJ. Spindle assembly checkpoint inhibition can resensitize p53-null stem cells to cancer chemotherapy. *Cancer Res* 2019;79:2392–403.
- 34 Lu G, Qiu Y, Su X. Targeting CXCL12-CXCR4 signaling enhances immune checkpoint blockade therapy against triple negative breast cancer. *Eur J Pharm Sci* 2021;157:105606.
- 35 Light may improve immune checkpoint blockade response. *Cancer Discov* 2016;6:OF9.
- 36 Yin L, Xue J, Li R, *et al.* Effect of low-dose radiation therapy on Abscopal responses to Hypofractionated radiation therapy and anti-PD1 in mice and patients with non-small cell lung cancer. *Int J Radiat Oncol Biol Phys* 2020;108:212–24.
- 37 Zhang W, Wang H, Sun M, *et al.* CXCL5/CXCR2 axis in tumor microenvironment as potential diagnostic biomarker and therapeutic target. *Cancer Commun* 2020;40:69–80.
- 38 Liu G, Rui W, Zheng H, *et al.* CXCR2-modified CAR-T cells have enhanced trafficking ability that improves treatment of hepatocellular carcinoma. *Eur J Immunol* 2020;50:712–24.
- 39 Voron T, Colussi O, Marcheteau E, *et al.* Vegf-A modulates expression of inhibitory checkpoints on CD8+ T cells in tumors. *J Exp Med* 2015;212:139–48.
- 40 Lapeyre-Prost A, Terme M, Pernet S, *et al.* Immunomodulatory activity of VEGF in cancer. *Int Rev Cell Mol Biol* 2017;330:295–342.
- 41 Kim CG, Jang M, Kim Y, *et al.* Vegf-A drives TOX-dependent T cell exhaustion in anti-PD-1-resistant microsatellite stable colorectal cancers. *Sci Immunol* 2019;4. doi:10.1126/sciimmunol.aay0555. [Epub ahead of print: 08 11 2019].
- 42 Chen J, Xun J, Yang J, *et al.* Plasma indoleamine 2,3-dioxygenase activity is associated with the size of the human immunodeficiency virus reservoir in patients receiving antiretroviral therapy. *Clin Infect Dis* 2019;68:1274–81.
- 43 Mitchell TC, Hamid O, Smith DC, *et al.* Epcadostat plus pembrolizumab in patients with advanced solid tumors: phase I results from a multicenter, open-label phase I/II trial (ECHO-202/KEYNOTE-037). *J Clin Oncol* 2018;36:3223–30.
- 44 Long GV, Dummer R, Hamid O, *et al.* Epcadostat plus pembrolizumab versus placebo plus pembrolizumab in patients with unresectable or metastatic melanoma (ECHO-301/KEYNOTE-252): a phase 3, randomised, double-blind study. *Lancet Oncol* 2019;20:1083–97.

Figure S1

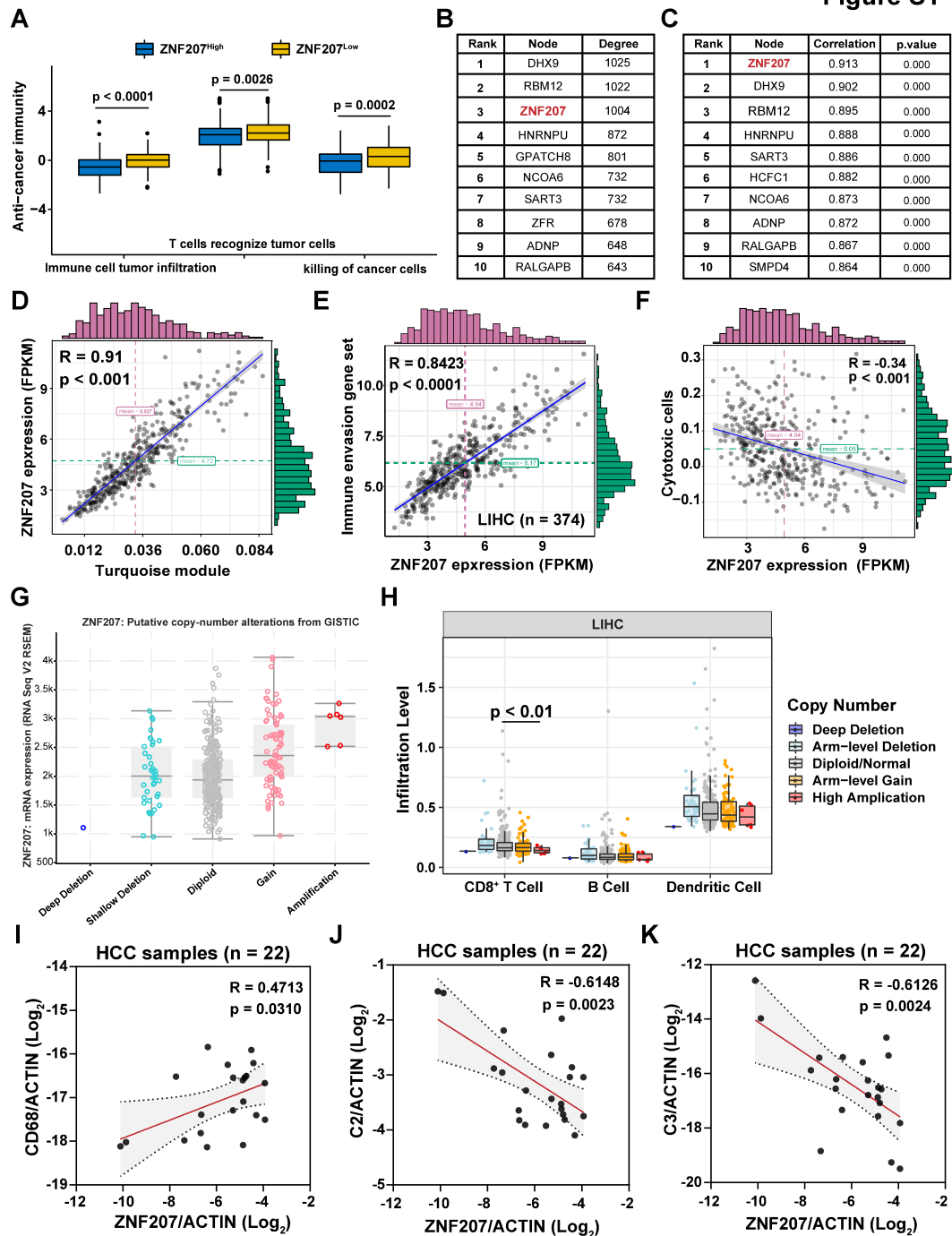
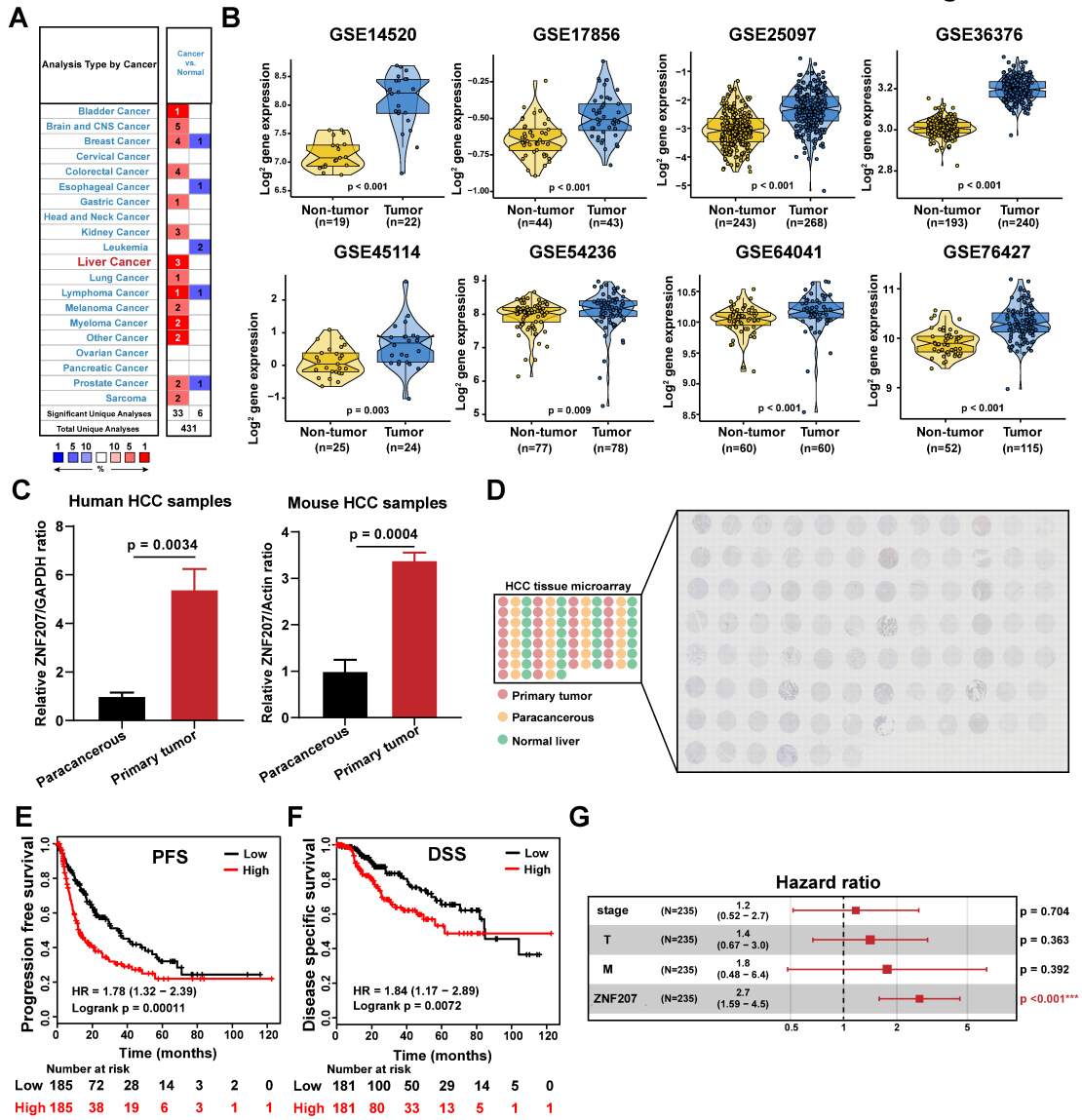


Figure S2



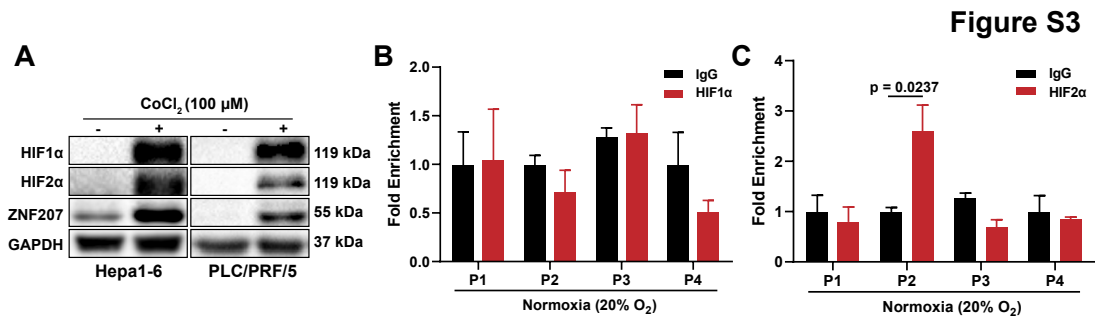


Figure S4

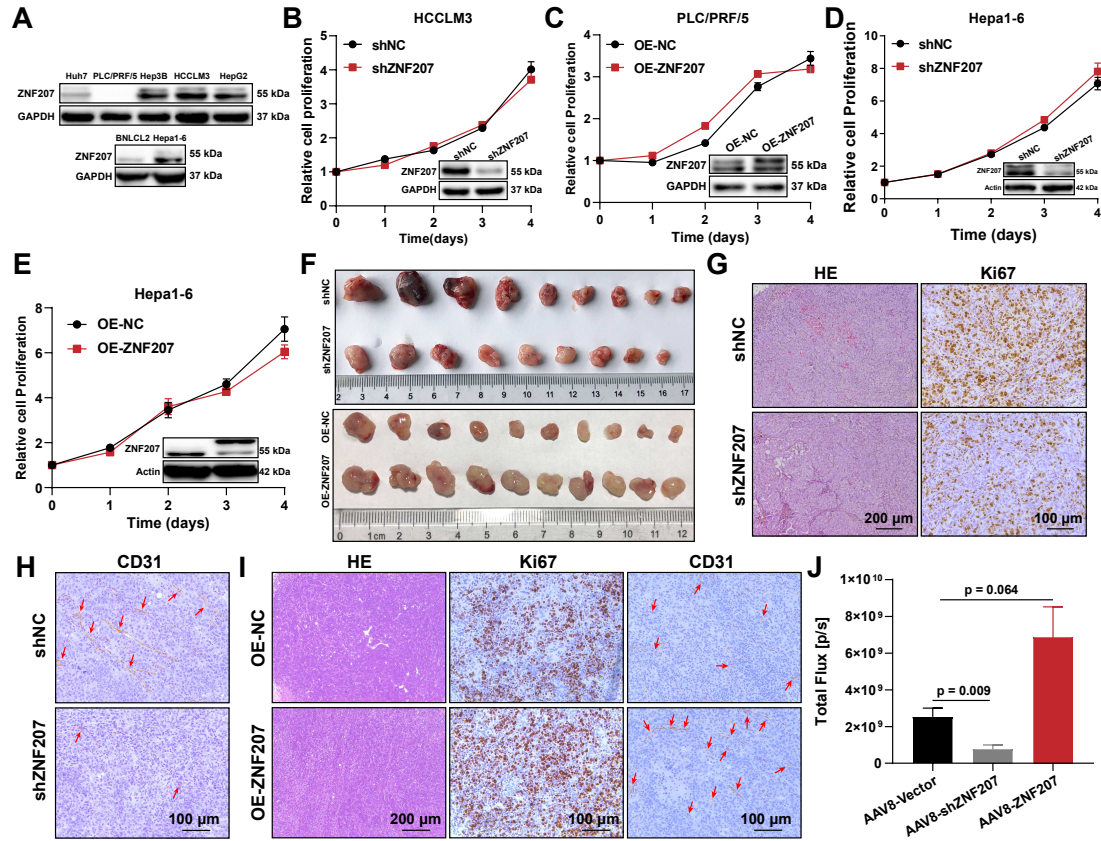


Figure S5

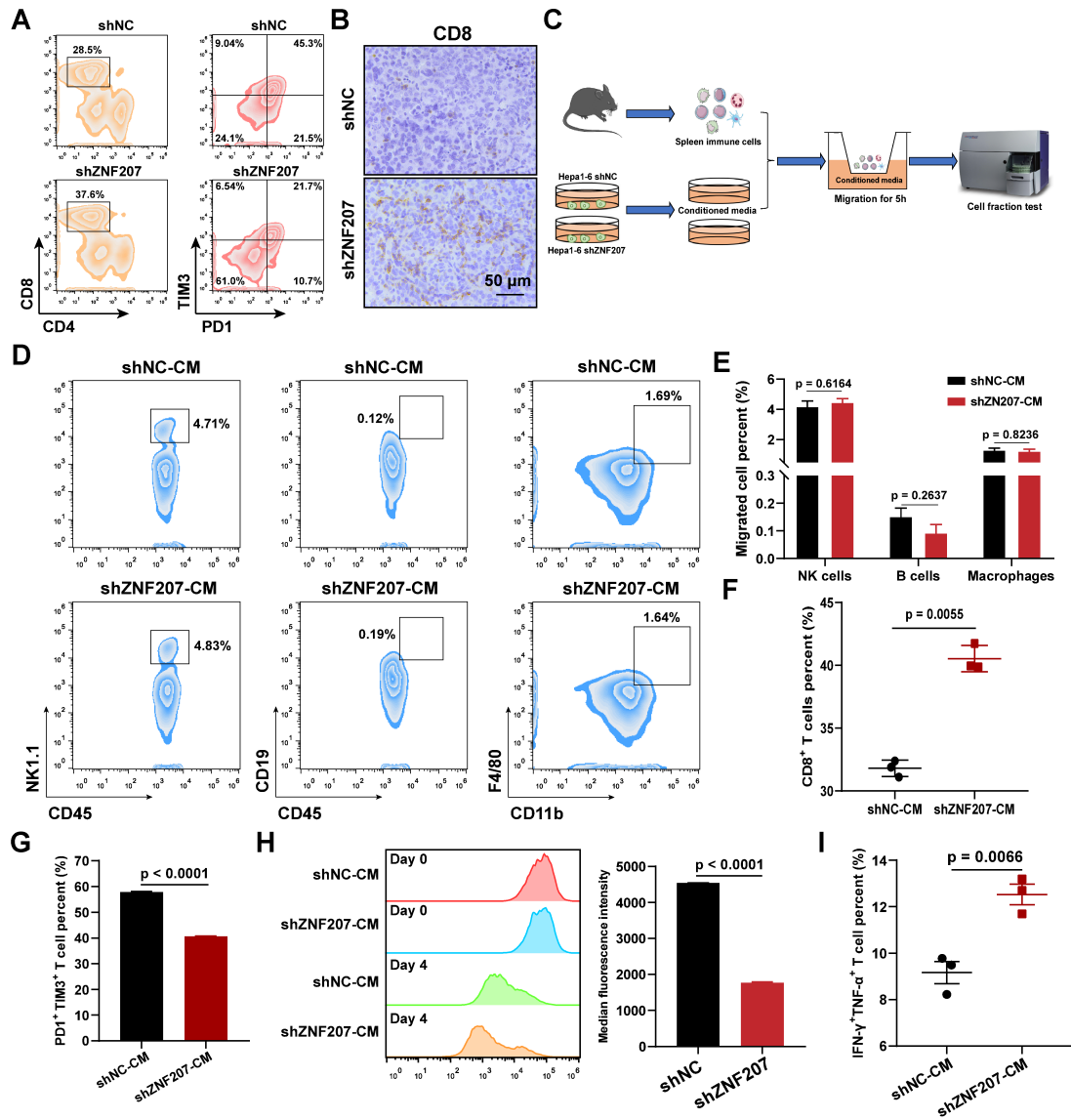
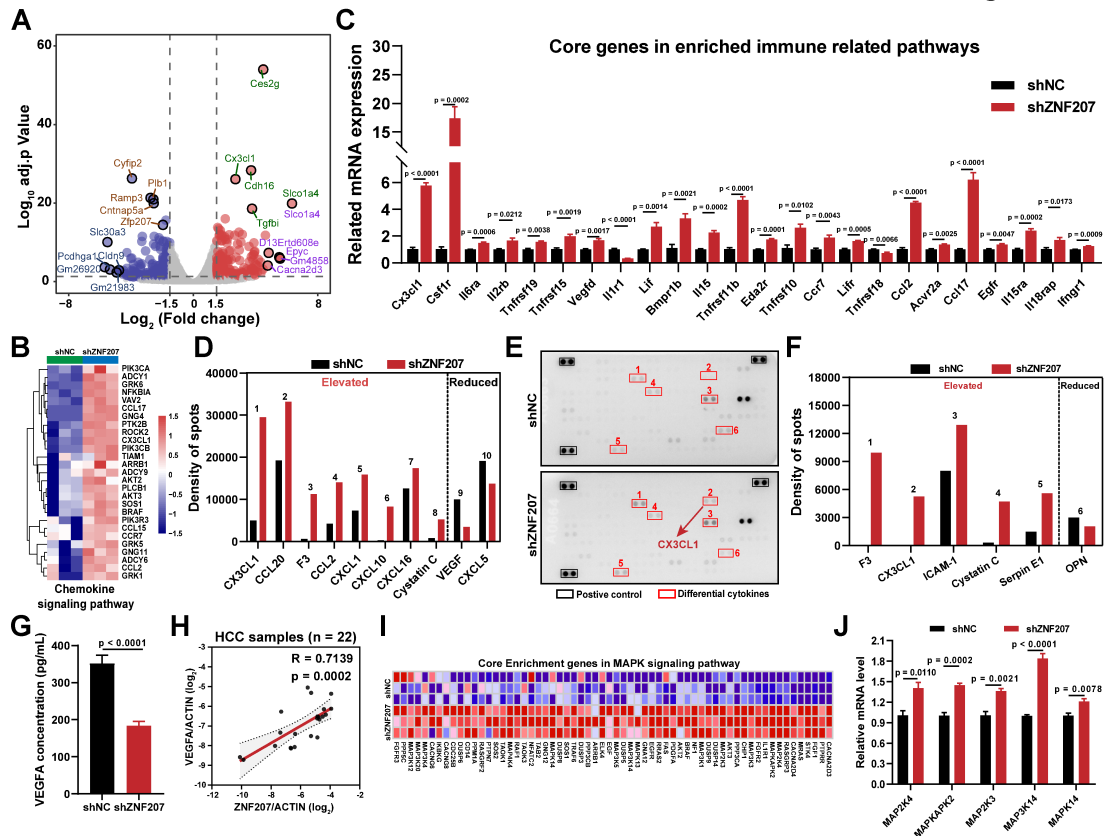


Figure S6



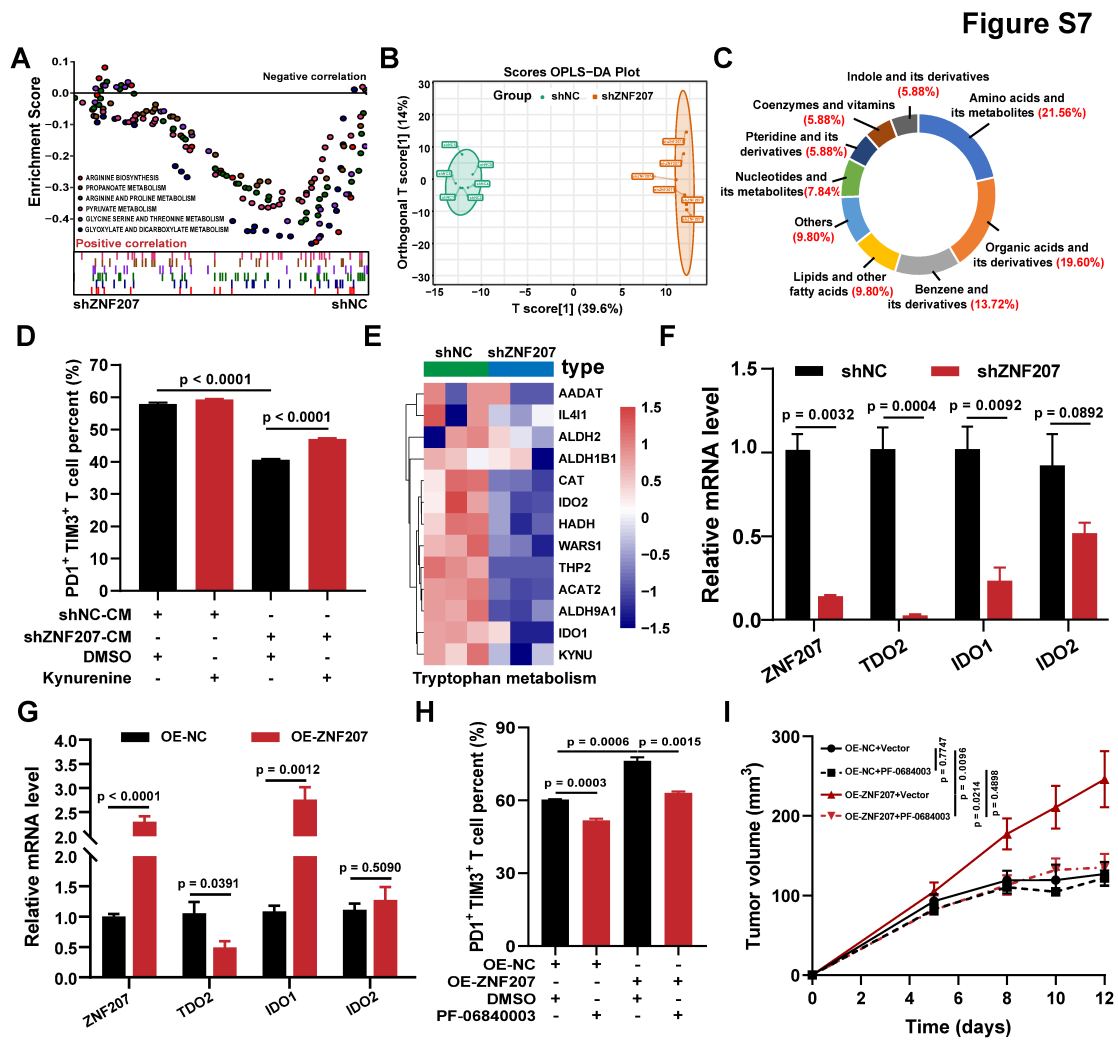


Figure S8

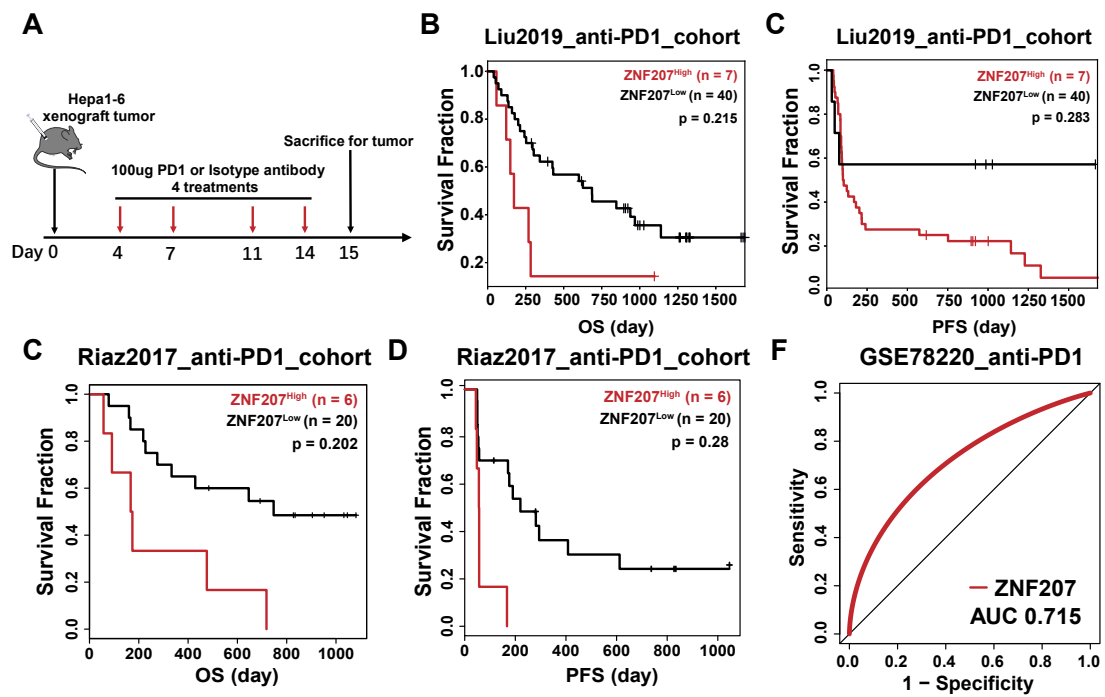


Figure S9

Figure 2E

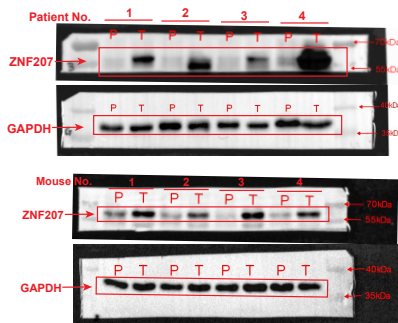


Figure 3B

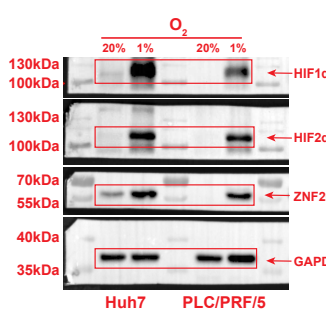


Figure S3A-Left

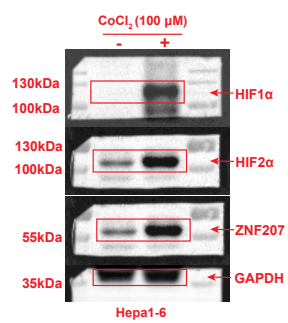


Figure S3A-Right

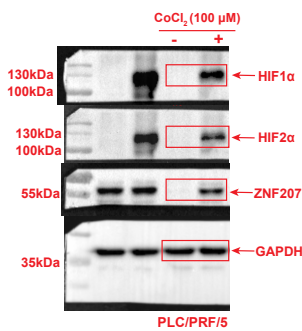


Figure 3C

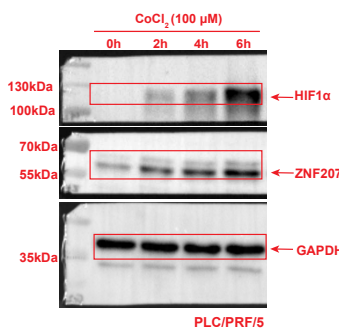


Figure 3D



Figure 3E

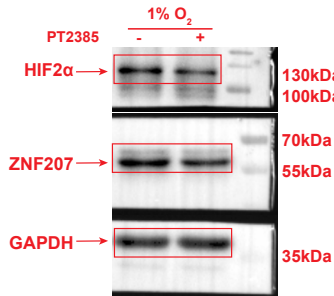


Figure 3F

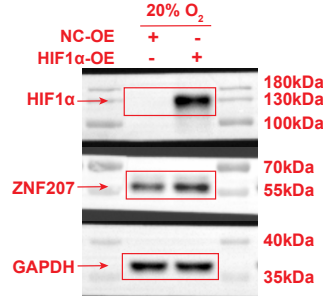


Figure 3G

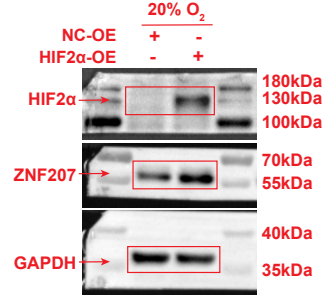


Figure S4A

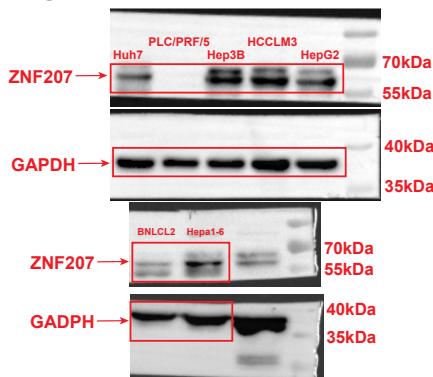


Figure S4B

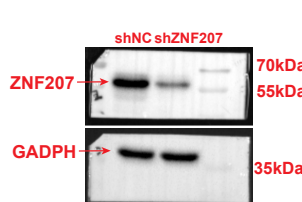


Figure S4C



Figure S4D

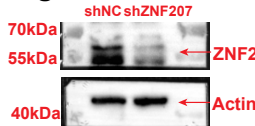
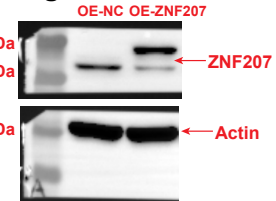


Figure S4E



23 **Supplementary Figures legends**

24 **Figure S1: ZNF207 is a potential immunosuppressive target in HCC.** (A) Box
25 diagram compared the cancer-immunity cycle scores from 5 to 7 steps in ZNF207^{high}
26 and ZNF207^{low} groups (grouped by the median value of ZNF207). (B) The 10 nodes
27 with the highest degree value in protein-protein interaction network. (C) The 10 genes
28 with the highest correlation with the turquoise module. (D) Scatter plot shows the
29 correlation between ZNF207 expression and turquoise module. (E) Correlation between
30 ZNF207 and cancer immune escape gene signature. (F) The scatter plot shows the
31 correlation between cytotoxic T cell abundance and ZNF207 expression in HCC
32 samples. (G) Scatter plots of copy number variations and ZNF207 expression levels.
33 (H) Scatter plot of CD8⁺ T cell, B cells and Dendritic Cells infiltration and ZNF207
34 copy number variation in HCC. (I-K) Scatter plot shows the correlation between
35 ZNF207 and multiple immune cell markers (CD68, C2 and C3), as determined by RT-
36 qPCR in 22 HCC samples. $|R| > 0.3$, $p < 0.05$ represents a significant correlation (n=22).
37

38 **Figure S2: ZNF207 is highly expressed in HCC and is associated with poor**
39 **prognosis.** (A) Oncomine database was used to analyze differential expression levels
40 of ZNF207 in all tumors. Red represents elevated expression while blue represents
41 suppressed expression levels. The numerical value represents data sets meeting the
42 screening conditions. (B) Violin plots show ZNF207 expression in cancer and normal
43 tissues of 8 HCC datasets from the GEO database (Sample numbers as shown in figure).
44 (C) Quantitative results of ZNF207 protein expression levels in human HCC and DEN

45 induced mouse HCC samples (n=4). (D) Expression of ZNF207 in primary tumor (n =
46 30), paracancerous (n=30) and normal tissues in HCC tissue microarray (n=30). (E-F)
47 The KM database was used to evaluate the relationship between ZNF207 and prognosis
48 of HCC patients, including PFS and DSS. (G) Forest plots based on multivariable
49 survival analysis of HCC patients.

50

51 **Figure S3: Hypoxia elevates ZNF207 in HCC.** (A) Western blot was used to detect
52 protein expression levels of ZNF207 in HCC cells (Hepa1-6 and PLC/PRF/5) treated
53 with CoCl₂ for 12 h. ChIP-qPCR was used to detect (B) HIF1 α and (C) HIF2 α
54 enrichment on the ZNF207 promoter under normoxia conditions.

55

56 **Figure S4: ZNF207 promotion of HCC is associated with tumor immunity.** (A)
57 Baseline protein levels of ZNF207 in HCC cell lines. (B-C) *In vitro* proliferation curve
58 of ZNF207 knockdown and overexpression in two human HCC cell lines (HCCLM3
59 and PLC/PRF/5) (n=6). (D-E) *In vitro* proliferation curve of ZNF207 knockdown and
60 overexpression in Hepa1-6 (n=6). (F) Image of ZNF207 knockdown and
61 overexpression subcutaneous xenograft tumors. (G-H) HE, ki67 and CD31 staining of
62 ZNF207 knockdown xenograft tumor tissue. (I) HE, ki67 and CD31 staining of
63 ZNF207 overexpression xenograft tumor tissue. (J) Fluorescence intensity quantitative
64 statistics of liver orthotopic intervention model treated with different AAV8 (n=8).

65

66 **Figure S5: ZNF207 promotes HCC associated CD8⁺ T cell infiltration and**

67 **exhaustion.** (A) Flow cytometry shows the percentage of CD8⁺ T cells and exhausted
68 CD8⁺ T cells in tumor tissues (n=10). (B) CD8⁺ T cell fractions in tumor tissues were
69 detected by immunohistochemistry. (C) Schematic presentation of the experimental
70 design of conditioned medium mediated immune cell chemotaxis. (D) Flow cytometry
71 was used to detect NK cells, B cells and macrophages chemotaxis when treated with
72 conditioned medium from ZNF207 knockdown cells (n=3). (E) Quantitative results of
73 flow cytometry analysis (n=3). (F) Quantitative results of CD8⁺ T cell percentage in
74 conditioned medium chemotaxis experiment (n=3). (G) Exhausted CD8⁺ T cell
75 percentage after treatment with ZNF207 knockdown cell conditioned medium (n=3).
76 (H) Proliferation of CD8⁺ T cells after treatment with ZNF207 knockdown cell
77 conditioned medium for 96 h (n=3). (I) IFN- γ ⁺ TNF- α ⁺ CD8⁺ T cell percentage when
78 treated with ZNF207 knockdown conditioned medium for 19 h (n=3).

79

80 **Figure S6: ZNF207 inhibits CD8⁺ T cells infiltration through MAPK-CX3CL1 axis.**

81 (A) Volcano plot of differentially expressed genes (DEGs), red represents up-regulated
82 genes, blue represents down-regulated genes, while gray represents not significantly
83 changed. (B) Gene expression heatmap of chemokine signaling pathway. (C) RT-qPCR
84 was used to detect mRNA expression levels of core genes in the immune pathways
85 (n=4). (D) Quantitative results of the 10 most significant cytokines as determined by
86 the cytokine antibody chip assay. (E) Detection of 111 cytokines in cell lysates of
87 ZNF207 knockdown Hepa1-6 cells. (F) Quantitative results of the six most
88 differentially expressed cytokines in cell lysates. (G) Concentration of CX3CL1 in the

89 ZNF207 knockdown conditioned medium was determined by ELISA (n=4). (H) Scatter
90 plot shows the correlation between ZNF207 and CX3CL1 in 22 HCC samples, $|R|>0.3$,
91 $p<0.05$ represents a significant correlation (n=22). (I) Heatmap of MAPK signaling
92 pathway enriched in Hepa1-6-shZNF207 group. (J) RT-qPCR was used to detect mRNA
93 expression levels of core genes in the MAPK pathways (n=6).

94

95 **Figure S7: ZNF207 promotes CD8⁺ T cell exhaustion by increasing kynurenine**
96 **levels.** (A) GSEA presentation of metabolic signaling pathways. (B) Orthogonal PLS-
97 DA (OPLS-DA) diagram of metabolomic analysis. (C) Proportional circle diagram of
98 differential metabolites. (D) Conditioned medium from ZNF207 knockdown cells was
99 supplemented with 10uM kynurenine and treated with CD8⁺ T cells for 48h, exhaustion
100 CD8⁺ T cells was quantified (n=3). (E) Expression heat map of core genes in the
101 tryptophan signaling pathway after ZNF207 knock down (n=3). (F) RT-qPCR verified
102 mRNA expression levels of core genes for kynurenine metabolism (n=4). (G) mRNA
103 expression levels of IDO1, IDO2 and TDO2 determined after transfecting PLC/PRF/5
104 cells with ZNF207 over expression plasmid (n=4). (H) CD8⁺ T cells were treated with
105 the conditioned medium from ZNF207 overexpression cells pre-treated with DMSO
106 and PF-0684003 (2 μ M) for 48h, percentage of exhausted CD8⁺ T cells were counted
107 (n=3). (I) *In vitro* proliferation curve of ZNF207 overexpression group treatment with
108 IDO1 inhibitor PF-0684003 (600mg/kg) in subcutaneous xenograft (n=10).

109

110 **Figure S8: ZNF207 is a potential combination target for anti-PD1 therapy.** (A)

111 Schematic presentation of *in vivo* animal experiments to test effects of ZNF207
112 knockdown combined with PD1 monoclonal antibody treatment (n=7). (B-E) Kaplan-
113 Meier survival curves of overall survival and progress free survival for patients with
114 high and low ZNF207 expression levels in the Liu2019_anti-PD1 and
115 Riaz2017_antiPD1 cohort from the TIDE database. ZNF207 low and high expression
116 groups were divided by best separation algorithm. (F) Predictive value of ZNF207,
117 measured by ROC curves in the GSE78220_anti-PD1 cohort.

118

119 **Figure S9: Original source data of the blotting images.**

120

121

122

123

124

125

126

127

128

129

130

131

132

133 **Supplementary Materials and methods**

134 **Immune score calculation based on ssGSEA algorithm**

135 We adopted a previously described procedure to determine the infiltration of immune
136 cells in LIHC dataset. In brief, we obtained the marker gene set for 24 immune cell
137 types from Zhang et al^{1,2}. Then the ssGSEA algorithm in the R package GSVA was
138 used to quantify the infiltration level of 24 immune cell types, and the immune
139 infiltration heatmap was drawn using the ggplot2 and pheatmap packages.

140

141 **Clinical indices analysis**

142 First, using the liver cancer data (TCGA-LIHC) in the TCGA database to analyze the
143 differential expression of ZNF207 in 50 matched cancer and para-cancerous samples.
144 Then, the OncomineTM database (<https://www.oncomine.org/>) was used to compare the
145 expression of ZNF207 in HCC and normal tissues. The p value was set to $P \leq 0.01$, the
146 fold change was set to 1.5, and meet the top 10% of the differential expression genes.
147 For the analysis of clinical indices, HCC samples were divided into high and low groups
148 according to median expression level of ZNF207, and the chi-square test was used to
149 analyze the relationship between ZNF207 and clinical indices, such as Tumor stage,
150 Tumor Grade, T, N, M stages, $p < 0.05$ indicates a significant statistical difference.

151

152 **Gene enrichment analysis**

153 For the enrichment analysis of the core genes in the selected modules, the ClueGO plug
154 in Cytoscape was used for analysis and graphical. The subsequent GSEA enrichment

155 analysis was performed as previous described³. GSEA software was downloaded from
156 the GSEA (<http://www.gsea-msigdb.org/gsea/index.jsp>), and the version number is:
157 GSEA_4.0.3. Default settings of GSEA software were used (1000 permutations). A
158 gene set with FDR < 0.25 was considered enriched. P-value and normalized enrichment
159 score (NES) were used to rank the enriched pathways in each phenotype. The hallmark,
160 KEGG, GO and other signatures used for enrichment analysis were download from the
161 Molecular Signatures Database (MsigDB,
162 <http://software.broadinstitute.org/gsea/index.jsp>). R software (version: R x64 3.6.0)
163 and Cytoscape software (version: 3.2.1) were used for graphical.

164

165 **Survival analysis**

166 First, the prognostic data of the ‘TCGA-LIHC’ dataset from TCGA database was used
167 to analyze the relationship between ZNF207 expression and patient prognosis (Overall
168 survival and Disease-free survival), and then the Kaplan-Meier Plotter database⁴
169 (<http://kmpplot.com/analysis/>) was used to verify the relationship between ZNF207
170 expression and HCC patient prognosis (including Overall Survival, Progression Free
171 Survival, Relapse Free Survival and Disease Free Survival). The survival analysis was
172 carried by Kaplan–Meier survival analysis and used the log-rank test, P < 0.05 was
173 regarded as statistically significant.

174

175 **Correlation analysis**

176 The correlation analysis involved in this study mainly includes two categories, the first

177 is the correlation between ZNF207 expression level and liver cancer immune
178 infiltration scores. Another is gene expression correlation between ZNF207 and other
179 genes. All correlation analyses were calculated using Pearson's method. $P < 0.01$, $|R| >$
180 0.5 indicates a strong correlation; $p < 0.05$, $|R| > 0.2$ indicates a correlation.

181

182 **Univariate and multivariate Cox model analysis**

183 Based on the clinical information of HCC patients, univariate analysis was performed
184 for survival-associated factors using the log rank test. For survival-associated factors
185 with a P value < 0.1 in univariate analysis. Then, factors with P value < 0.1 were
186 selected for multivariate analyses using the Cox regression model to identify the
187 prognostic-associated factors in HCC, P value < 0.05 in multivariate analyses can be
188 identified as independent prognostic indicator.

189

190 **Clinical sample collection and preparation**

191 Fresh hepatocellular carcinoma tissues were obtained from Nanjing Drum Tower
192 Hospital (Nanjing, China). The studies were approved by the ethical committee of
193 Nanjing Drum Tower Hospital (Nanjing, China).

194

195 **Cell lines and cell culture**

196 HEK293T, H22-luc, HCCLM3 were purchased from Nanjing Kezhen Biological Co.,
197 Ltd (Nanjing, China). Hepa1-6 and PLC/PRF/5 were purchased from National
198 Collection of Authenticated Cell Cultures (Shanghai, China). HEK293T, HCCLM3,

199 Hepa1-6 were cultured in DMEM (Biological Industries, Cat. No. 01-052-1A)
200 supplemented with 10% FBS (Biological Industries, Cat. No. 04-001-1A) and 1%
201 pen/strep (Hyclone, Cat. No. SV30010). H22-luc, PLC/PRF/5 was cultured in RPMI
202 1640 (Biological Industries, Cat. No. 01-100-1A) with 10% FBS and 1% pen/strep. All
203 cell lines were authenticated by STR (Short Tandem Repeat) profiling and confirmed
204 to lack of mycoplasma using the GMyc-PCR Mycoplasma Test Kit (YeSen, Shanghai,
205 China, 40601ES10). All cells were grown in a humidified incubator at 37 °C, 5% CO₂.

206

207 **Lentivirus infection and stable line establishment.**

208 Lentiviruses were produced and used to infect human cell lines as previously described⁵.
209 In short, the shRNA construct and the third-generation packaging vector (pMD2.G,
210 pMDLg/pRRE and pRSV-Rev) were co-transfected into HEK293T cells using the
211 DNA transfection reagent *Polyplus-transfection*[®]. The lentiviral particles were
212 harvested 72 hours after transfection and directly added to target cells together with 8
213 µg/ml polybrene. After two rounds of infection, the cells were screened with a medium
214 containing 3 µg/ml puromycin and passaged at least three times, and the protein and
215 mRNA levels were verified by western blot and RT-qPCR respectively. ZNF207
216 overexpression lentivirus was ordered from Shanghai Genechem Co., Ltd., and used
217 similar methods to infect and screen cells.

218

219 **RNA extraction and quantitative RT-PCR analysis.**

220 Total RNA was isolated using the Trizol reagent (Takara) and quantified by UV

221 spectrophotometry. For analysis of mRNA expression, 500 ng of RNA was reverse-
222 transcribed into first-strand cDNA using the HiScript II Q RT SuperMix for qPCR
223 (+gDNA wiper) (Takara, Cat. No. R223-01). Quantitative real-time PCR (qPCR) was
224 performed using Cham QTM Universal SYBR qPCR Master Mix (Takara, Cat. No.
225 Q711-02). Primer sequences were listed in Supplementary Table 2. mRNA expression
226 was normalized to reference gene Actin using the $\Delta\Delta\text{Ct}$ method.

227

228 **Protein extraction and immunoblotting.**

229 For total protein extraction, the cells were washed 3 times with ice-cold PBS and lysed
230 in a radioimmunoprecipitation assay (RIPA) buffer (Thermo Scientific, USA). Add
231 phosphatase inhibitor and protease inhibitor (Thermo Scientific, USA) at 1:100
232 according to the manufacturer's instructions. Based on spectrophotometry (Thermo
233 Scientific, USA), the concentration of protein lysate was determined using Pierce BCA
234 Protein Assay Kit. After centrifugation at 12000×g for 10 minutes at 4°C, the
235 supernatant was collected for subsequent protein electrophoresis. Take 15-30 ug protein
236 supernatant, use loading buffer for denaturation, and separate the protein by SDS-
237 PAGE (10%-12% gradient). The separated protein was transferred to a PVDF
238 membrane (Merck Millipore, USA), the membrane was blocked in Tris-buffered saline
239 (TBS) containing 5% skimmed milk powder for 2 hours, and incubated with the
240 indicated primary antibodies overnight at 4°C. Expose the membrane to a specific type
241 of horseradish peroxidase (HRP) conjugated secondary antibody, and then use an
242 enhanced chemiluminescence solution (ECL, Thermo Scientific, USA) for detection.

243

244 **Flow cytometry.**

245 **(1) Detection of immunocytes in tumor tissue.** 0.5 g tumor tissue was taken and
246 minced with gentle MACSTM Octo Dissociator (Miltenyi Biotec, Germany) and
247 digested in RPMI-1640 media (Biological Industries, Israel) containing 0.25 mg/mL
248 Collagenase D (Roche, Mannheim, Germany) and 0.1 mg/mL DNase I (Sigma, USA).
249 The digested cell suspension was then washed with PBS and filtered through a 70 µm
250 cell strainer. According to standard flow cytometry procedures, block with 5% BSA for
251 30 minutes, then stain with dead-living dye for 30 minutes, and finally stain with the
252 corresponding antibody for 30 minutes on ice at 4°C in the dark, wash with PBS and
253 test by the flow cytometer.

254 **(2) Chemotaxis of immune cells.** Separate mouse spleen cells, filter them with a 70
255 µm filter, and incubate them with red blood cell lysate at room temperature for 2
256 minutes. After stopping the lysis, wash twice with PBS. After staining with trypan blue,
257 use serum-free RPMI 1640 (Biological Industries, Cat. No. 01-100-1A) to adjust the
258 cell density to 5×10^6 cell/mL. A transwell chamber with a diameter of 24 mm and a
259 filter membrane pore size of 8 µm was used to perform immune cell chemotaxis
260 experiments. Add 1.5 mL of spleen single cell suspension to the upper chamber, add
261 2.6 mL of control conditioned medium and ZNF207 knockdown conditioned medium
262 to the lower chamber. After culturing for 5 hours, collect the cells in lower chamber
263 medium, and follow the standard flow cytometric staining procedure.

264 **(3) Intracellular staining.** The rapidly proliferating CD8⁺ T cells were cultured in

265 Hepa1-6-shNC conditioned medium and Hepa1-6-shZNF207 conditioned medium for
266 19 hours, and then 10 ng/mL phorbol ester 12-myristate 13-acetate (PMA) and 2 ug/mL
267 ionomycin were administered, BD Golgi&Stop™ also be added at 1:1000 at the same
268 time, stimulate the culture for 5h and collect the cells for flow cytometry staining. Fc
269 Block was added to each sample at a ratio of 1 ug/10⁶cells, block at 4°C for 15 minutes,
270 then stain for surface markers, then use Fixation/Permeabilization solution for rupture
271 treatment, and finally use Perm/Wash™ Buffer to configure cells Internally stained
272 flow cytometry antibodies, including: IFN- γ and TNF- α .

273 **(4) T cell proliferation.** The rapidly proliferating CD8⁺ T cells were pretreated with
274 0.1 μ M CFSE, and then cultured in Hepa1-6-shNC and Hepa1-6-shZNF207
275 conditioned medium (supplemented with 200 U/mL IL2) for 96 h, then collected T cells
276 to detect the proliferation of CD8⁺ T cells.

277 **(5) T cell exhaustion assay in vitro.** CD8⁺ T cells were activated with 1ug/mL
278 CD3/CD28 antibody for 48 h, 200 U/mL IL2 was used for expansion and culture for 3
279 days, and then 0.1 ug/mL CD3/CD28 antibody was used to stimulate T cells again for
280 48h, and conditioned medium was given at the same time to test the effect of
281 conditioned medium on CD8⁺ T cells exhaustion.

282 Cells were stained with fluorescently conjugated antibodies: LIVE/DEAD™ Fixable
283 far-red dead cell stain kit (Invitrogen, Cat. No. L10119), LIVE/DEAD™ Fixable Violet
284 dead cell stain kit (Invitrogen, Cat. No. L34964), CD45 (APC-Cy7, Clone: 30-F11,
285 Biolegend, Cat. No. 103116), CD11b (BV510, Clone: M1/70, Biolegend, Cat. No.
286 101263), F4/80 (APC, Clone: BM8, Biolegend, Cat. No. 123116), CD45 (BV510,

287 Clone: 30-F11, Biolegend, Cat. No. 103138), CD3e (PE-CY7, Clone: 145-2C11,
288 Biosciences, Cat. No. 552774), CD4 (FITC, Clone: RM4-5, Biolegend, Cat. No.
289 100510), CD8 (PE, Clone: 53-6.7, Biolegend, Cat. No. 100708), PD1 (APC, Clone:
290 RMP1-30, Biolegend, Cat. No. 109112), TIM3 (BV421, Clone: RMT3-23, Biolegend,
291 Cat. No. 119723), CD19 (APC-Cy7, Clone: MB19-1, molecular probes, Cat. No.
292 A15391), NK1.1 (APC, Clone: PK136, Biolegend, Cat. No. 108710), CD27 (PE, Clone:
293 LG.3A10, Biolegend, Cat. No. 124210), IFN- γ (FITC, Clone: XMG1.2, Invitrogen, Cat.
294 No. RM9001), TNF- α (APC, Clone: MP6-XT22, Biolegend, Cat. No. 506308).
295 CellTrace™ CFSE Cell Proliferation Kit (FITC, Thermofisher, Cat. No. C34554). Cells
296 were detected by the BD FACSVerser™ Flow Cytometer (BD, USA) and were analyzed
297 by FlowJo Software.

298

299 **Luciferase reporter assay.**

300 PLC/PRF/5 cells (1×10^6 cells/well) were grown in a 6-well plate for 24 hours, and 1.5
301 μ g ZNF207-promoter-pGL3-Basic dual luciferase reporter plasmid or vector-pGL3-
302 Basic control plasmid and 0.2 μ g pRL-TK-Renilla plasmid was co-transfected for 24h,
303 placed in a hypoxic incubator, cultured for 24h under the conditions of 1% O₂, 5% CO₂
304 and 37°C, or added CoCl₂ (1 mM) for 12h. For IDO1 promoter reporter assay, promoter
305 plasmids were co-infected with ZNF207 overexpression plasmid for 48h. Then used
306 Dual Luciferase Reporter Assay Kit (Vazyme) and full-wavelength microplate reader
307 (PerkinElmer) measured the fluorescence values of firefly luciferase and Renilla
308 luciferase. Renilla luciferase was used as an internal reference to calibrate transfection

309 efficiency to eliminate differences in cell number and transfection efficiency between
310 wells. All plasmids were purchased from Changsha YouBio Biological Co., Ltd.

311

312 **Cell viability assay**

313 For cell viability assay, cells were seeded into 96-well plates at a density of 0.7×10^4
314 cells per well. Cell viability was measured using the CCK8 assay.

315

316 **Histologic staining**

317 The tissue was fixed in 4% paraformaldehyde for 7 days, embedded in paraffin, cut into
318 4 μm thick sections, and then stained with hematoxylin and eosin (H&E). For
319 immunohistochemical staining, the array of tissue chip was gained from commercial
320 company (Shanghai Superchip Biotech, Shanghai, China) containing 30 paired HCC
321 specimens. paraffin sections were deparaffinized with xylene and rinsed with ethanol.
322 Recover the antigen by boiling the slices in EDTA buffer. The sections were stained
323 with the primary antibody at 4°C overnight, and then the horseradish peroxidase-
324 conjugated secondary antibody was stained at room temperature for 30 minutes. The
325 sections were developed with 3,3'-diaminobenzidine (Sigma-Aldrich) and
326 counterstained with hematoxylin. For histological analysis, the deparaffinized sections
327 were counterstained with hematoxylin and eosin.

328

329 **RNA-sequencing**

330 Total RNA was extracted using TRIZOL Reagent (Life technologies) following the

331 manufacturer's instructions and checked for a RIN number to inspect RNA integrity
332 using an Agilent Bioanalyzer 2100 (Agilent technologies). Qualified total RNA was
333 further purified by RNAClean XP Kit (Beckman) and RNase-Free DNase Set
334 (QIAGEN). 1 µg - 3 µg of total RNA was subsequently used to prepare RNA-seq
335 libraries using TruSeq RNA Sample Pre-Kit v2 (Illumina), Agencourt® AMPure XP
336 Beads (Beckman), SuperScript II Reverse Transcriptase (Invitrogen), Qubit™ dsDNA
337 HS Assay Kit (Invitrogen) and Qubit™ dsDNA HS Assay Kit (Invitrogen) following
338 the manufacturers' protocols. The libraries were paired-end sequenced with HiSeq
339 2500 (Illumina). The RNA-seq data in this manuscript has been deposited in NCBI's
340 Gene Expression Omnibus and is accessible with the accession number: GSE167935.

341

342 **ELISA**

343 Mouse CX3CL1/Fractalkine Quantikine ELISA Kit (Cat. No. MCX310) was purchased
344 from R&D (Emeryville, CA, USA). KYN (Kynurenine) ELISA Kit (Cat. No. EU0188)
345 was purchased from FineTest (Wuhan, China). All used according to the manufactures'
346 instructions.

347

348 **UPLC-MS/MS-Based Metabolite Detection and Data Processing.**

349 Metabolites from the Hepa1-6-shNC and Hepa1-6-shZNF207 were determined via
350 UPLC-MS/MS, according to a previous study⁶. Briefly, the UPLC system (Shim-pack
351 UPLC SHIMADZU CBM30A), combined with an MS/MS system (QTRAP 6500+),
352 was set at a resolution of 30,000 to obtain UPLC-MS/MS statistics. Sample analysis

353 was conducted in positive ion modes, with a spray voltage of 5.5 kV and negative ion
354 modes, with a spray voltage of -4.5 kV and a capillary temperature of 500 °C. The mass
355 scanning scope was set from 50 m/z to 1500 m/z . Nitrogen sheath and nitrogen auxiliary
356 gas were set at 30 L/min and 10 L/min, respectively. Solvent A was 0.04% acetic acid
357 (Fisher Scientific)/water (Millipore) (v/v), and solvent B was 0.04% acetic
358 acid/acetonitrile (Fisher Scientific) (v/v). The gradient flow rate was 0.4 mL/min, and
359 the column temperature was 40 °C. The process was as described below: 5% B at 0 min,
360 95% B at 11.0 min, 95% B at 12.0 min, 5% B at 12.1 min, and 5% B at 14 min. The
361 QC samples were injected four times at the start to ensure system consistency. A Waters
362 ACQUITY UPLC HSS T3 C18 column (100 mm × 2.1 mm, 1.8 μm) was used for all
363 analyses. Sample was thawed on ice, then added 1 mL pre-cooled extractant (70%
364 methanol aqueous solution), and whirl for 1 min. Freeze the mixture for 3 min in liquid
365 nitrogen after remove ice for 3 min, it will be whirled for 2 min, circulate this at 3 times.
366 Centrifuge the mixture again with 12000 r/min at 4°C for 10 min. Finally take the
367 supernatant into the sample bottle for LC-MS/MS analysis.

368

369 **Immunotherapeutic response prediction**

370 Referring to the previous study⁷, according to the expression level of ZNF207, the liver
371 cancer samples of TCGA were divided into two groups: ZNF207^{Low} (Bottom 10%) and
372 ZNF207^{High} (Top 10%), and then the TIDE algorithm (<http://tide.dfci.harvard.edu/>) and
373 submap algorithm from the GenePattern website (<https://cloud.genepattern.org/gp>)
374 were used to predicts the sensitivity of the two groups samples to PD1 monoclonal

375 antibody and CTLA4 monoclonal antibody treatment. TIDE is a calculation method
376 that uses gene expression profiles to predict ICB response. It evaluates two different
377 tumor immune escape mechanisms, including the dysfunction of tumor-infiltrating
378 cytotoxic T lymphocytes (CTL) and the rejection of CTL by immunosuppressive
379 factors⁸. SubMap was used to compare the similarity of expression profiles; this feature
380 can be reflected as a treatment response⁹.

381

382 **Statistical analysis.** All data analyses were done using GraphPad Prism 8 or SPSS
383 version 19. Two-tailed student's t test was performed when only 2 groups were
384 compared. The paired T test was used in the analysis of the difference in ZNF207
385 expression between 50 paired HCC samples. One-way ANOVA followed by Dunnett's
386 posttests were used to compare differences between multiple groups unless otherwise
387 stated. The chi-square test was used to analyze the relationship between ZNF207 and
388 clinical indices. Pearson's analysis was used in correlation analysis. Kaplan-Meier
389 analysis was used in survival analysis. *P < 0.05, **P < 0.01, ***P < 0.001.

390

391 **Reference**

- 392 1. Zhang L, Zhao Y, Dai Y, et al. Immune Landscape of Colorectal Cancer Tumor
393 Microenvironment from Different Primary Tumor Location. *Front Immunol* 2018;9:1578.
- 394 2. Bindea G, Mlecnik B, Tosolini M, et al. Spatiotemporal dynamics of intratumoral immune
395 cells reveal the immune landscape in human cancer. *Immunity* 2013;39:782-95.
- 396 3. Wu H, Zhang J. Decreased expression of TFAP2B in endometrial cancer predicts poor

- 397 prognosis: A study based on TCGA data. *Gynecol Oncol* 2018;149:592-597.
- 398 4. Menyhart O, Nagy A, Gyorffy B. Determining consistent prognostic biomarkers of overall
399 survival and vascular invasion in hepatocellular carcinoma. *R Soc Open Sci* 2018;5:181006.
- 400 5. Huang H, Weng H, Zhou K, et al. Histone H3 trimethylation at lysine 36 guides m(6)A RNA
401 modification co-transcriptionally. *Nature* 2019;567:414-419.
- 402 6. Xiao Y, Li X, Zeng X, et al. A Low omega-6/omega-3 Ratio High-Fat Diet Improves Rat
403 Metabolism via Purine and Tryptophan Metabolism in the Intestinal Tract, While Reversed
404 by Inulin. *J Agric Food Chem* 2019;67:7315-7324.
- 405 7. Lu X, Jiang L, Zhang L, et al. Immune Signature-Based Subtypes of Cervical Squamous
406 Cell Carcinoma Tightly Associated with Human Papillomavirus Type 16 Expression,
407 Molecular Features, and Clinical Outcome. *Neoplasia* 2019;21:591-601.
- 408 8. Jiang P, Gu S, Pan D, et al. Signatures of T cell dysfunction and exclusion predict cancer
409 immunotherapy response. *Nat Med* 2018;24:1550-1558.
- 410 9. Hoshida Y, Brunet JP, Tamayo P, et al. Subclass mapping: identifying common subtypes
411 in independent disease data sets. *PLoS One* 2007;2:e1195.
- 412
- 413
- 414
- 415
- 416
- 417

418 **Supplementary Table 1:** Univariate and multivariable Cox model analysis for the
 419 prognostic effects of ZNF207 based on the TCGA Liver cancer dataset.

| Characteristics | Univariate Cox | | | | Multivariate Cox | | | |
|-----------------|----------------|--------|-------|---------------|------------------|--------|-------|--------------|
| | Hazard Ratio | 95% CI | | p-Value | Hazard Ratio | 95% CI | | p-Value |
| | | Lower | Upper | | | Lower | Upper | |
| Age | 1.005 | 0.697 | 1.608 | 0.5912 | - | - | - | - |
| Gender | 0.780 | 1.015 | 2.362 | 0.3013 | - | - | - | - |
| Grade | 1.017 | 1.945 | 4.466 | 0.9143 | - | - | - | - |
| Stage | 1.865 | 1.609 | 6.029 | 0.0000 | 1.172 | 0.518 | 2.651 | 0.704 |
| T | 1.804 | 2.618 | 6.242 | 0.0000 | 1.413 | 0.670 | 2.979 | 0.363 |
| M | 3.850 | 1.580 | 3.915 | 0.0228 | 1.760 | 0.482 | 6.427 | 0.392 |
| N | 2.022 | 2.159 | 5.132 | 0.3276 | - | - | - | - |
| ZNF207 | 3.216 | 1.332 | 3.1 | 0.0000 | 2.681 | 1.589 | 4.524 | 0.000 |

420

421

422

423

424

425

426

427

428

429

430

431

432

433

434

435

Supplementary Table 2: The primers have been used for real time PCR.

| Gene | Primer sequences (5'-3') |
|-------------|---------------------------------|
| hAADAT-F | AAGACTGCCGTAATCACTGTAGA |
| hAADAT-R | ACTCGGAGAATACTGAAGTGCTC |
| hACAT2-F | CTTTAGCACGGATAGTTTCCTGG |
| hACAT2-R | GCTGCAAAGGCTTCATTGATTTC |
| hActin-F | GCGTGACATTAAGGAGAAG |
| hActin-R | GAAGGAAGGCTGGAAGAG |
| hC2-F | CCTTGAATGGGAGCAAACCTGAAC |
| hC2-R | GATTGATGTGAAAGTCTCGTGGC |
| hC3-F | GCTGCTCCTGCTACTAACC |
| hC3-R | AAAGGCAGTTCCTCCACTTT |
| hCD3G-F | GGAATCTGGGAAGTAATGCCAA |
| hCD3G-R | TCAATGCAGTTCTGACACATTCT |
| hCD4-F | CTTCTGGTGCTGCAACTGG |
| hCD4-R | GCTGTACAGGTCAGTTCC |
| hCD86-F | CTGCTCATCTATACACGGTTACC |
| hCD86-R | GGAAACGTCGTACAGTTCTGTG |
| hCD8A-F | CTTACCAGTGACCGCCTTG |
| hCD8A-R | CACTTCAGCTCCACTGTCTC |
| hCD11b-F | ACTTGCAGTGAGAACACGTATG |
| hCD11b-R | TCATCCGCCGAAAGTCATGTG |
| hCX3CL1-F | GCCACAGGCGAAAGCAGTA |
| hCX3CL1-R | GGAGGCACTCGGAAAAGCTC |
| hFOXP3-F | GTGGCCCGGATGTGAGAAG |
| hFOXP3-R | GGAGCCCTTGTCGGATGATG |
| hGAPDH-F | CCTTCATTGACCTCAACTAC |
| hGAPDH-R | GAAGATGGTGATGGGATTTC |
| hIDO1-F | GATGTCCGTAAGGTCTTGCC |
| hIDO1-R | TCCAGTCTCCATCACGAAAT |
| hIDO2-F | CATAGCAAGGAAAGTGGTGAC |
| hIDO2-R | CTAACCACGTGGGTGAAGGATTG |
| hVEGFA-F | AGGGCAGAATCATCACGAAGT |
| hVEGFA-R | AGGGTCTCGATTGGATGGCA |
| hZNF207-F | TAGATGCCGTACCAAATGCAAT |
| hZNF207-R | GTCGTCGTCTTTCATCCATGT |
| mAADAT-F | ATGAATTACTCACGGTTCCTCAC |
| mAADAT-R | AACATGCTCGGGTTTGGAGAT |
| mACAT2-F | CCCGTGGTCATCGTCTCAG |
| mACAT2-R | GGACAGGGCACCATTGAAGG |
| mActin-F | ACCACACCTTCTACAATGAG |
| mActin-R | ACGACCAGAGGCATACAG |

| | |
|------------|-------------------------|
| mAcvr2a-F | GCGTTCGCCGTCTTTCTTATC |
| mAcvr2a-R | GTTGGTTCGTCTCTTTCCCAAT |
| mALDH9A1-F | GGCCGAGTGATTGCCACTT |
| mALDH9A1-R | AGGCCACTTTTCTTACTCCAGA |
| mBmpr1b-F | CCTCGGCCCAAGATCCTAC |
| mBmpr1b-R | CCTAGACATCCAGAGGTGACA |
| mCcl2-F | TTAAAAACCTGGATCGGAACCAA |
| mCcl2-R | GCATTAGCTTCAGATTTACGGGT |
| mCcl17-F | TACCATGAGGTCACTTCAGATGC |
| mCcl17-R | GCACTCTCGGCCTACATTGG |
| mCcr7-F | TGTACGAGTCGGTGTGCTTC |
| mCcr7-R | GGTAGGTATCCGTCATGGTCTTG |
| mCsf1r-F | TGTCATCGAGCCTAGTGGC |
| mCsf1r-R | CGGGAGATTCAGGGTCCAAG |
| mCx3cl1-F | ACGAAATGCGAAATCATGTGC |
| mCx3cl1-R | CTGTGTCTGTCTCCAGGACAA |
| mEda2r-F | CACACTGCATAGTCTGCCCTC |
| mEda2r-R | GCCTTCTGGACCCGATTGA |
| mEgfr-F | GCCATCTGGGCCAAAGATACC |
| mEgfr-R | GTCTTCGCATGAATAGGCCAAT |
| mGAPDH-F | AGTGGCAAAGTGGAGATT |
| mGAPDH-R | GTGGAGTCATACTGGAACA |
| mIDO1-F | GCCTCCTATTCTGTCTTATGCAG |
| mIDO1-R | ATACAGTGGGGATTGCTTTGATT |
| mIDO2-F | CCAGAAGGACCGTTGGAAATC |
| mIDO2-R | ACTGTCACTAGGATGAAGCCC |
| mIfngr1-F | CTGGCAGGATGATTCTGCTGG |
| mIfngr1-R | GCATACGACAGGGTTCAAGTTAT |
| mIl1r1-F | GTGCTACTGGGGCTCATTTGT |
| mIl1r1-R | GGAGTAAGAGGACACTTGCGAAT |
| mIl2rb-F | TGGAGCCTGTCCCTCTACG |
| mIl2rb-R | TCCACATGCAAGAGACATTGG |
| mIl6ra-F | CCTGAGACTCAAGCAGAAATGG |
| mIl6ra-R | AGAAGGAAGGTCGGCTTCAGT |
| mIl15-F | ACATCCATCTCGTGCTACTTGT |
| mIl15-R | GCCTCTGTTTTAGGGAGACCT |
| mIl15ra-F | CGTGTCCACCTCCCGTATCTA |
| mIl15ra-R | AGACATACTCTCCCTGGAGT |
| mIl18rap-F | AGACTACTTCTGAGCACAAGA |
| mIl18rap-R | TGTCCTTACCAATGGTTCTCACT |
| mLif-F | ATTGTGCCCTTACTGCTGCTG |
| mLif-R | GCCAGTTGATTCTTGATCTGGT |
| mLifr-F | TACGTCCGCAGACTCGATATT |
| mLifr-R | TGGGCGTATCTCTCTCTCCTT |

| | |
|--------------|-------------------------|
| mTnfsf10-F | GGGAGTCCTCTCGGAAAGG |
| mTnfsf10-R | CCGGATAGCTGGTGTACTTGTA |
| mTnfrsf11b-F | CAGAGAAGCCACGCAAAAGTG |
| mTnfrsf11b-R | AGCTGTGTCTCCGTTTTATCCT |
| mTnfsf15-F | AGTCCCAGTGGAAGTGCTG |
| mTnfsf15-R | GTGCTAAGTCCTGCGAGGAT |
| mTnfrsf18-F | GCCATGCTGTATGGAGTCTCG |
| mTnfrsf18-R | CCACTTCCGTTCTGAACCTTG |
| mTnfrsf19-F | TTCTGTGGGGGACACGATG |
| mTnfrsf19-R | AGAAAATTCAGCGCAGATGGAA |
| mVEGFA-F | AGGGCAGAATCATCACGAAGT |
| mVEGFA-R | AGGGTCTCGATTGGATGGCA |
| mVegfd-F | TTGAGCGATCATCCCGGTC |
| mVegfd-R | GCGTGAGTCCATACTGGCAAG |
| mWARS1-F | GCTGGAAATGCACCAAAGATG |
| mWARS1-R | GCTTGTCCGCACTGTCCAT |
| mZfp207-F | AGCAAGGTTATATCCCACCAATG |
| mZfp207-R | AGGAACACCTGGCATCAATGG |
| mMAP2K4-F | AATCGACAGCACGGTTTACTC |
| mMAP2K4-R | TGAAATCCCAGTGTTGTTTCAGG |
| mMAPKAPK2-F | TTCCCCCAGTTCCACGTCA |
| mMAPKAPK2-R | GCAGCACCTTCCCGTTGAT |
| mMAP2K3-F | GCCTCAGACCAAAGGAAAATCC |
| mMAP2K3-R | GGTGTGGGGTTGGACACAG |
| mMAPK14-F | GGCTCGGCACACTGATGAT |
| mMAPK14-R | TGGGGTTCCAACGAGTCTTAAA |
| mMAP3K14-F | TGTGGGAAGTGGGAGATCCTA |
| mMAP3K14-R | GGCTGAACTCTTGGCTATTCTCA |

436

437

438

439

440

441

442

443

Supplementary Table 3. The primers have been used for Chip-qPCR.

| Gene Promotor | Primer sequences (5'-3') |
|----------------------|--|
| IDO1-P1-F | TGAACTGATTCCCAAAGTATTAGCCTCATG |
| IDO1-P1-R | AGCTCTCGCGCTATTCTCTACTAAAT |
| IDO1-P2-F | TGCTGTATAATTTTGGTTTCAGTTTTCCCTTACATTT |
| IDO1-P2-R | ACTTGAAATAAATTAATTTGTGATAGCATATGGCTTTTCG |
| IDO1-P3-F | AGCGCGAGAGCTATTCTAGACT |
| IDO1-P3-R | ATGATCAAAAGGAGAAAAGAGAAATAGTTCGTG |
| ZNF207-P1-F | GATTACAGGCGTGCCCCAC |
| ZNF207-P1-R | CCTGTAATCCCAGCACTGTGGG |
| ZNF207-P2-F | ACTACGCCTGGCTAATTTTTGTATTTTTAGTAGAG |
| ZNF207-P2-R | GTAAGACTGGAGCTGATAGCCGG |
| ZNF207-P3-F | ATCAGCTCCAGTCTTACCACGAT |
| ZNF207-P3-R | AAGCAAGGTGAAGGAAAGGGTATCT |
| ZNF207-P4-F | TGCTTCCTGTGGGACGTGG |
| ZNF207-P4-R | TTCTACCGGCAAAGTAAAAGGGAGG |

444